Saturated absorption and crossover resonances in a high-finesse cavity: Formalism and application to the hyperfine structure of jet-cooled NO₂ by saturated-absorption cavity-ring-down spectroscopy

Patrick Dupré[*]

Department of Chemistry, University of York, Heslington, York YO10 5DD, United Kingdom
(Received 6 October 2011; published 4 April 2012)

The $^q R_0(0)$ rotational transition in the $\widetilde{A}\,^2B_2 \longleftarrow \widetilde{X}\,^2A_1$ system of jet-cooled NO₂ located around $12\,536$ cm^{-1} is analyzed using a nonlinear-susceptibility formalism designed to describe the saturated absorption due to two identical counter-propagating radiations in an n-level system. An analytical solution of the equations of motion is obtained in the frequency space by considering the pertinent experimental conditions, mainly a high-finesse cavity and a slit-shaped supersonic expansion. Calculation of the nonlinear absorption coefficient requires the summing of all Zeeman-component contributions and a final numerical integration over the frequency detuning assuming a Maxwell-Boltzmann speed distribution. Determination of the experimental absorption coefficients is obtained by converting the shape of the temporal decay of the electromagnetic field amplitude initially captured inside the cavity. The molecular Hamiltonian includes both spin-rotation and hyperfine interactions. Molecular constants relative to the upper level are derived by exploiting Doppler-broadening-free so-called saturated-absorption cavity-ring-down spectroscopy. The dipole moment of the partially assigned hot band is obtained [$\mu_{\mathrm{band}} = 0.0047(12)$ D] together with the number density and the effective population relaxation rates. The model is validated by varying the intracavity power from 0 to 230 W (i.e., up to a maximum peak irradiance of 240×10^3 W/cm^2), representing saturation coefficients up to 120. The experimental position, shape, and width of the Lamb and crossover dips are well reproduced. The spatial shape and modulation of the electromagnetic field are discussed.

I. INTRODUCTION

Since the 1960s, the saturated-absorption (SA) phenomenon in the gas phase has focused attention because it easily allows reaching a Doppler-broadening-free spectral resolution when two counter-propagating laser beams impinge on the species under study. It was first observed in gas lasers and was seen as an undesirable effect [1–5]. Then it was promoted as a very convenient technique to get around Doppler broadening [6] and has become a noteworthy implement for metrology and high-resolution spectroscopy purposes [7–9]. However, because it is basically a nonlinear process requiring distinction of at least two components of the electromagnetic (EM) field, the determination of the intensity and shape of the transitions requires, one way or another, a nonlinear susceptibility tensor component to be calculated. The recent advent and diffusion of high-finesse optical cavities (such as those used for cavity-ring-down spectroscopy; CRDS) have created new interest in accurately exploiting this nonlinear effect. The high intensity of the EM field, which can be captured inside such cavities, allows examination of molecular transitions under saturation exhibiting even a moderate absorption cross section. To the author's best knowledge, the first SA spectrum showing a Lamb dip by using the CRDS technique was reported for nitrogen dioxide [10]. Unsurprisingly, nonlinear absorption breaks the usual exponential ring-down (RD) temporal decay. Instead, nonexponential decays can be quantitatively analyzed if decent control of the captured beam shape and intensity is supplied [11]. Although nonexponential decays have been reported several times in the past, their analysis may remain difficult because of the possible combined effects of the

saturation and of the broad spectral extension of the radiation source (pulsed CRDS) compared with the molecular transition [12–14]. With the use of continuous-wave (cw)-CRDS, in 2000, weak Lamb dips were reported for ethylene in the 10-μm range [15] and then by Hodges's group for gaseous water [16,17], but none of these authors mentioned nonexponential decay. More recently, Lamb dips exhibiting the hyperfine structure of ^{17}O^{12}C^{16}O have been reported [18], as well as the associated nonexponential decays. A tentative analysis of nonexponential decays has been published by Lee and Hahn [19], using a rate-equation-based model.

Because Doppler-broadening-free SA involves two counter-propagating waves, nonstatic particles can experience two distinct EM fields, each one characterized by an opposed Doppler frequency shift (the recoil effects [20] are ignored here). Hence a given molecule can simultaneously absorb over two different transitions (i.e., at two different frequencies), raising additional crossover resonances [21–29]. If two transitions share a same energy level (requiring consideration of a three-level system) and if their frequency difference does not exceed the molecular Doppler broadening (along the velocity component interrogated), they will interfere. This behavior needs to be distinguished from the case where two transitions do not share a common level (e.g., the case of two independent two-level systems), giving rise to a crossover dip whose amplitude differs from that due to the interfering transitions.

The radical NO₂ has a long spectroscopic history for several reasons: (i) it absorbs in the visible spectral range, (ii) it is an atmospheric constituent, and (iii) it offers rich and complex spectroscopy. The NO₂ spectrum is relatively well understood up to $\sim 10\,000$ cm^{-1} [30]; however, above this energy, a conical intersection [31,32] strongly perturbs

*patrick.dupre@york.ac.uk

the vibrational structure and, possibly, the rotational structure. Only jet-cooling conditions combined with double-resonance spectroscopy allowed an extended vibrational identification [30,33]. Rotational spectroscopy can also suffer from such an interaction, providing dispersed values of the rotational constants when analysis by frequency difference combinations are performed [34,35]. Fortunately, the vibrationless ground state is now well documented and the fine and hyperfine tensor components have been available to a high accuracy since the 1960s, thanks to microwave studies [36–38].

Hyperfine structures of NO_2 in state $\widetilde{A}\,^2B_2$ were first observed by Demtröder and collaborators in 1974, at around 19 435 cm^{-1} (detection by fluorescence) [39], thanks to a skimmed jet expansion and a high-resolution laser source (resolution limited to 20 MHz). Recently, using a similar jet expansion combined with bolometric detection (residual linewidth of 12 MHz) [40–42], a more extensive study of the Fermi contact term focused on the vibronic mixture of the upper state for bands located between 11 200 and 13 680 cm^{-1}. The quantum beat technique is also an alternative way to determine hyperfine structures; the accuracy of the gap determination between the level energies is independent of the spectral resolution of the laser source [43].

The present paper combines data obtained with a supersonic slit-shaped expansion residing inside a CRDS cavity and a relevant modeling of the SA. SA is only observable if the absorption cross sections are large enough; for jet-cooled NO_2 currently only hot vibronic bands, issued from the vibrational mode ν_2 (bent), match such a condition. Presently, we report on one rotational transition $^qR_0(0)$, located around 12 536 cm^{-1} and belonging to a band previously identified as strong [35]. Fine and hyperfine interactions split this transition into nine components, which are all observable, thanks to the Doppler-free technique considered here. Attempts to assign the rest of the band have failed until now.

We show that the combination of a crude slit expansion with the cw-CRDS technique is almost optimal for study of SA (so-called SA-CRDS), if full control of the injected beam is obtained. This includes control of the spatial extension and intensity of the intracavity beam and accurate monitoring of the temporal decay. The SA-CRDS technique conveniently combines the triple advantages of (i) the sensitivity of detection attached to the absorption enhancement due to the high-finesse cavity, (ii) being Doppler broadening–free, and (iii) being a self-calibrated absorption technique. Contrary to the traditional absorption techniques measuring beam intensity attenuation, the CRDS technique assesses cavity optical losses through its characteristic time [44]. In the limit of linear (i.e. weak) absorption, the RD time provides a straightforward measurement of the absorption coefficient, independently of the intensity of the EM field.

We have developed a semiclassical formalism based on the density matrix in the frequency space and analytically solved a set of coupled equations for a given value of the frequency detuning. Initially applied to a three-level system, it has been extended to an n-level system. The cross-coherence matrix elements have been ignored and argued. The specific case of noninterfering transitions is also discussed. The population

relaxation rates are basically assumed to be controlled by the transit time. However, this assumption can be loose since the transit time limits only the observable population relaxation rate. It allows one to ignore complications due to a nonmonochromatic EM field. Actually, the model should only be valid for low saturation coefficients because the harmonic contributions of the impinging frequencies [45] have been neglected. A complete spectral simulation is obtained by a single numerical integration and by summing up all the Zeeman components. It turns out that the experimental line profiles, including nonlinear resonances (i.e., crossover resonances), have been accurately simulated. In addition, with the purpose of simultaneously determining the band strength and the number density, fits of the absorption dependence versus the intracavity power have been performed. We conclude that the model applies to saturation coefficients as high as 120. Furthermore, some features of supersonic expansion are discussed, such as the residual Doppler broadening and the number density of NO_2 radicals seeded in the jet expansion. The values of the Fermi contact interaction, of one term of the electronic-spin nuclear-spin dipole interaction, of the spin-rotation constant $\overline{\overline{\epsilon}}_{bb}$, and of the "band origin" $T_0' + B' + C'$ are given for the unassigned upper vibronic level.

Calculation of the nonlinear absorption coefficient (scalar) is based on a "nonperturbative" approach in the limit of moderate absorption. This means that the absorbed EM field modifies the population of the lower and upper levels by pumping but is not itself altered by the absorption process. This calculation deviates from perturbative approaches commonly used to calculate the third-order susceptibility tensor when a pump and a probe beam can be distinguished [46–48]. Here, the role of both interfering EM fields is permutable (both pump and probe beams are identical), which gives a high symmetry to the problem.

The Mulliken modified notation is used to assign the spin-rotation (or fine) structure [49–52]. When the hyperfine structure must be addressed, lower and upper values of the total angular momentum F are indicated (J-scheme of coupling [53]), as well as the relevant Wang symmetry. Otherwise, the asymmetric top nomenclature is used.

II. DENSITY-MATRIX FORMALISM

The scalar nonlinear susceptibility is sought using the formalism of the density matrix. The density-matrix elements are unknown quantities, while the molecular Hamiltonian, the relaxation matrix elements, and the populations in the absence of an external EM field are the given quantities. The density-matrix elements are coupled quantities and no analytical solutions are available without approximation, which is discussed. Performing the calculations in the frequency space raises some changes compared with calculations in the time space, typically in the physical dimension of the quantities utilized. However, to avoid cumbersome notation, the usual notation is used. Moreover, when a variable (typically the frequency detuning) is listed as an argument of a function, it may be simply removed from the argument list after integration, without further notice.

A. Liouville equation and level system

The Liouville equation in the time space is given by [54]

$$
\frac{\partial \widehat{\rho}(t,\boldsymbol{r})}{\partial t} = -\frac{i}{\hbar}[H_0 + \widehat{V}(t,\boldsymbol{r}),\widehat{\rho}(t,\boldsymbol{r})] - \frac{1}{2}\{\widehat{\rho}(t,\boldsymbol{r}),\Gamma_{\text{rel}}\} + \widehat{\Lambda}(t,\boldsymbol{r}), \quad (1)
$$

where H_0, $\widehat{\Lambda}$, and Γ_{rel} are diagonal matrices ([,] is the usual commutation operator, and {,} denotes the matrix-density relaxation). Γ_{rel} is the phenomenological relaxation matrix, H_0 is the molecular Hamiltonian in the absence of external interaction, $\widehat{V}(t,\boldsymbol{r})$ is the electric dipole interaction, and $\widehat{\Lambda}(t,\boldsymbol{r})$ is the molecule source term ($\boldsymbol{r}$ denotes the spatial coordinates).

We consider the interaction between an EM field and a molecular system inside a space free of a static field (i.e., magnetic or electric). The generic molecular eigenlevels are assigned by $|l X_l \kappa_l m_l\rangle$ and $|u X_u \kappa_u m_u\rangle$ to the lower and upper level, respectively. X denotes the total angular momentum, for example, N, J, or F, according to the internal coupling scheme, while m (the orientational quantum number) denotes its projection with respect to the laboratory-fixed quantization axis assigning the Zeeman magnetic sublevels; κ denotes the $2X + 1$ eigenvectors of the total angular momentum operator (u and l denoting any additional assignment if necessary).

In this approach, the level system is constituted of "one" lower level and several upper levels ("V"-shape configuration [22,55]). Hence u can run from 1 to the number of upper levels.

When dealing with linear absorption, usually the Zeeman sublevel structures can be partially ignored because all the dipole moment matrix elements of the Zeeman transitions (or subtransitions) are proportional to the reduced matrix element (Wigner-Eckart theorem), independent of the intensity of the EM field, and hence can be easily added by using a sum rule. In contrast, when considering nonlinear absorption, this sum rule does not apply because of the nonlinear EM-field dependence of the dipole moment matrix elements.

For the sake of simplicity, we also assume that all the Zeeman sublevels belonging to the same energy level have the same source terms, Λ_u or Λ_l, and that the subtransitions all have the same coherence (or transversal) damping rate γ_{ul}, given by

$$
\gamma_{ul} = \frac{\Gamma_u + \Gamma_l}{2} + \gamma_{\text{col}}, \quad (2)
$$

where γ_{col} is the collisional rate (no additional energy redistribution process is expected). The relevance of the population damping rates Γ_u and Γ_l is discussed in Sec. II C.

The time dependence of the differential Liouville equation can be Fourier transformed in the angular frequency space (i.e., ω) by using the usual transformation operations (see Appendix B). When considering only the spatial dependence along the z direction, Eq. (1) becomes

$$
i\omega\rho(\omega,z) = -\frac{i}{\hbar}[2\pi H_0 \delta(\omega) + V(\omega,z),\rho(\omega,z)]_{\otimes}
$$
$$
- \frac{1}{2}\{\rho(\omega,z),\Gamma_{\text{rel}}\} + \Lambda(\omega,z), \quad (3)
$$

where $[,]_{\otimes}$ is now the commutator including the relevant convolution products (denoted $\otimes$) and $\delta(\omega)$ is the Dirac δ function (see Appendix B).

B. Solutions of the Liouville equation in the frequency space for a three-level system (V-shape configuration)

The "three-level" system considered here is described by "one" lower level and "two" upper levels; the latter levels are not directly coupled together (i.e., $V_{12} = V_{21} = 0$). The "three-level" system is in fact a $[(2X_l + 1) + (2X_1 + 1) + (2X_2 + 1)]$–sublevel system composed of three blocks of degenerated levels. Each block being diagonal, the matrix can be treated like it is a pure three-level system by indexing the density and dipole moment matrix elements as m_l, m_1, and m_2 (or m_u), as mentioned earlier.

In the absence of an external EM field, molecule populations are governed by planar supersonic expansion [56], which can be characterized by its spatial localization (*viz.*, the absorbing volume), its molecular orientation/alignment [57], and the molecule speed distribution along the three spatial directions, v_x, v_y, and v_z. Assuming that the limit speed of the carrier gas has been reached during the expansion it comes $v_x = v_{\text{limit}}$ [56]. The component v_z gives rise to a Doppler shift (or frequency detuning) $\delta = \frac{\omega}{c}v_z$, while $v_y = 0$ (the latter hypothesis is re-examined in Sec. II G). The jet expansion is supposed to conserve the space isotropy (no molecular orientation or alignment is anticipated: $\sum_{m_l} m_l \rho_{m_l} = 0$). In addition, we assume that inside the expansion $\frac{\partial \rho_{ii}}{\partial z} \simeq 0$ ($i = l,u$).

Assuming Galilean invariance and ignoring recoil effects [58], solutions of the Liouville equation can be sought for a given frequency detuning (δ) by introducing the relevant quantities [e.g., see Eq. (24)]. Hence we get, for the populations,

$$
i\omega\rho_{m_u m_u}(\omega,z,\delta) = i[\rho_{m_l m_u}(\omega,z,\delta) \otimes \Omega_{m_u m_l}(\omega,z)
$$
$$
- \rho_{m_u m_l}(\omega,z,\delta) \otimes \Omega_{m_l m_u}(\omega,z)]
$$
$$
- \Gamma_u \rho_{m_u m_u}(\omega,z,\delta) + \Lambda_u(\omega,z,\delta), \quad (4)
$$

$$
i\omega\rho_{m_l m_l}(\omega,z,\delta) = i\sum_u [\rho_{m_u m_l}(\omega,z,\delta) \otimes \Omega_{m_l m_u}(\omega,z)
$$
$$
- \rho_{m_l m_u}(\omega,z,\delta) \otimes \Omega_{m_u m_l}(\omega,z)]
$$
$$
- \Gamma_l \rho_{m_l m_l}(\omega,z,\delta) + \Lambda_l(\omega,z,\delta), \quad (5)
$$

and, for the coherences,

$$
i\omega\rho_{m_u m_l}(\omega,z,\delta)
$$
$$
= -i\{(\omega_{ul} + \delta)\rho_{m_u m_l}(\omega,z,\delta) - [\rho_{m_l m_l}(\omega,z,\delta)
$$
$$
- \rho_{m_u m_u}(\omega,z,\delta)] \otimes \Omega_{m_u m_l}(\omega,z)
$$
$$
+ \rho_{m_u m_{u'\neq u}}(\omega,z,\delta) \otimes \Omega_{m_{u'\neq u} m_l}(\omega,z)\} - \gamma_{ul}\rho_{m_u m_l}(\omega,z,\delta), \quad (6)
$$

$$
i\omega\rho_{m_u m_{u'\neq u}}(\omega,z,\delta)
$$
$$
= i\{\omega_{u'u}\rho_{m_u m_{u'\neq u}}(\omega,z,\delta)
$$
$$
+ \rho_{m_l m_{u'\neq u}}(\omega,z,\delta) \otimes \Omega_{m_{u'\neq u} m_l}(\omega,z)
$$
$$
- \rho_{m_u m_l}(\omega,z,\delta) \otimes \Omega_{m_l m_{u'\neq u}}(\omega,z)\} - \gamma_{uu'}\rho_{m_u m_{u'\neq u}}(\omega,z,\delta), \quad (7)
$$

where Ω_{ij} is the Rabi frequency of the subtransition $[V_{ij}(\omega,z) = -\hbar\Omega_{ij}(\omega,z)]$, given by

$$
\Omega_{m_u \mu_l}(\omega,z,r) = \frac{|\mu_{m_u m_l}|}{\hbar} E(\omega,z,r). \quad (8)
$$

The term $\mu_{m_u m_l}$ is the dipole moment matrix element of the subtransition $|u X_u \kappa_u m_u\rangle \leftrightarrow |l X_l \kappa_l m_l\rangle$, and $E(\omega, z, r)$ is the Fourier transform of the temporal shape of the impinging EM field, whose spatial dependencies are discussed in Sec. II G. A slowly varying envelope approximation of the EM field is assumed. In the rotating-wave approximation (RWA), $\rho_{m_u m_l}(\omega, z, \delta) = \rho_{m_l m_u}^*(\omega, z, \delta)$.

The coherence terms, (6), and the so-called cross-coherence (also so-called two-photon coherence) terms, (7), provide couplings not only with the population terms but also between the coherence matrix elements. The cross-coherence terms $\rho_{m_u m_{u' \neq u}}(\omega, z, \delta)$, or, to simplify, the notation $\rho_{m_1 m_2}$, clearly play a specific role in the couplings between the coherences. It is appealing to set the cross-coherences to 0; the reader can find justification in Appendix A. This approximation allows us to deal with the approximated coherences:

$$
\begin{aligned}
i\omega\rho_{m_u m_l}(\omega, z, \delta) \\
= -i\{(\omega_{ul} + \delta)\rho_{m_u m_l}(\omega, z, \delta) \\
-[\rho_{m_l m_l}(\omega, z, \delta) - \rho_{m_u m_u}(\omega, z, \delta)] \otimes \Omega_{m_u m_l}(\omega, z)\} \\
-\gamma_{ul}\rho_{m_u m_l}(\omega, z, \delta).
\end{aligned}
\tag{9}
$$

By summing Eqs. (4) and (5), we get

$$
\begin{aligned}
i\omega\left[\rho_{m_l m_l}(\omega, z, \delta) + \sum_u \rho_{m_u m_u}(\omega, z, \delta)\right] \\
= -\Gamma_l \rho_{m_l m_l}(\omega, z, \delta) - \sum_u \Gamma_u \rho_{m_u m_u}(\omega, z, \delta) + \Lambda_l(\omega, z, \delta) \\
+ \sum_u \Lambda_u(\omega, z, \delta),
\end{aligned}
\tag{10}
$$

and by subtracting Eq. (4) from Eq. (5), we obtain

$$
\begin{aligned}
i\omega\left[\rho_{m_l m_l}(\omega, z, \delta) - \sum_u \rho_{m_u m_u}(\omega, z, \delta)\right] \\
= -2i\sum_u[\rho_{m_u m_l}(\omega, z, \delta) \otimes \Omega_{m_l m_u}(\omega, z) \\
-\rho_{m_l m_u}(\omega, z, \delta) \otimes \Omega_{m_u m_l}(\omega, z)] - \Gamma_l \rho_{m_l m_l}(\omega, z, \delta) \\
+ \sum_u \Gamma_u \rho_{m_u m_u}(\omega, z, \delta) + \Lambda_l(\omega, z, \delta) - \sum_u \Lambda_u(\omega, z, \delta).
\end{aligned}
\tag{11}
$$

Introducing the quantities

$$
\Gamma_{ul} = \frac{\Gamma_u + \Gamma_l}{2}
\tag{12}
$$

and

$$
\delta_{ul} = \frac{\Gamma_u - \Gamma_l}{2},
\tag{13}
$$

and assuming $\Gamma_1 = \Gamma_2 = \Gamma_u$, Eq. (10) can be recast as

$$
\begin{aligned}
\rho_{m_l m_l}(\omega, z, \delta) + \sum_u \rho_{m_u m_u}(\omega, z, \delta) \\
= -\frac{\delta_{ul}}{i\omega + \Gamma_{ul}}\left[\rho_{m_l m_l}(\omega, z, \delta) - \sum_u \rho_{m_u m_u}(\omega, z, \delta)\right] \\
+ \frac{\Lambda_l(\omega, z, \delta) + \sum_u \Lambda_u(\omega, z, \delta)}{i\omega + \Gamma_{ul}},
\end{aligned}
\tag{14}
$$

which can be substituted into (11) and gives the differential population inversion,

$$
\rho_{m_l m_l}(\omega, z, \delta) - \sum_u \rho_{m_u m_u}(\omega, z, \delta) = -\Lambda_l(\omega)\frac{1 - \frac{\delta_{ul}}{i\omega + \Gamma_{ul}}}{i\omega + \Gamma_{ul} - \frac{\delta_{ul}^2}{i\omega + \Gamma_{ul}}} - \sum_u \Lambda_u(\omega)\frac{1 + \frac{\delta_{ul}}{i\omega + \Gamma_{ul}}}{i\omega + \Gamma_{ul} - \frac{\delta_{ul}^2}{i\omega + \Gamma_{ul}}} + \rho\rho(\omega, z, \delta),
\tag{15}
$$

where

$$
\rho\rho(\omega, z, \delta) = -2i\frac{\sum_u[\rho_{m_u m_l}(\omega, z, \delta) \otimes \Omega_{m_l m_u}(\omega, z) - \rho_{m_l m_u}(\omega, z, \delta) \otimes \Omega_{m_u m_l}(\omega, z)]}{i\omega + \Gamma_{ul} - \frac{\delta_{ul}^2}{i\omega + \Gamma_{ul}}}.
\tag{16}
$$

By distinguishing the molecule traveling in each opposite direction ($\delta > 0$), Eq. (9) becomes

$$
\rho_{m_l m_u}^{(\pm)}(\omega, z, \delta) = \frac{1}{2}\frac{[\rho_{m_l m_l}(\omega, z, \delta) - \rho_{m_u m_u}(\omega, z, \delta)] \otimes \Omega_{m_l m_u}(\omega, z)}{\omega_{ul} - \omega \mp \delta + i\gamma_{ul}}.
\tag{17}
$$

The solution of the population matrix elements can be obtained from Eqs. (15) and (17) by solving a system of coupled equations for any frequency characterizing the impinging EM field when the initial level populations and source terms are known. They are carried out by expressing the two population inversions, $\rho_{m_l m_l}(\omega, z, \delta) - \rho_{m_1 m_1}(\omega, z, \delta)$ and $\rho_{m_l m_l}(\omega, z, \delta) - \rho_{m_2 m_2}(\omega, z, \delta)$, with respect to the population sums, $\rho_{m_l m_l}(\omega, z, \delta) + \rho_{m_1 m_1}(\omega, z, \delta)$ and $\rho_{m_l m_l}(\omega, z, \delta) + \rho_{m_2 m_2}(\omega, z, \delta)$. Both population inversions can be deduced by subtracting Eq. (4) from Eq. (5), yielding

$$
\begin{aligned}
i\omega\left[\rho_{m_l m_l}(\omega, z, \delta) - \rho_{\substack{m_1 m_1 \\ m_2 m_2}}(\omega, z, \delta)\right] = 2i\left[\rho_{\substack{m_1 m_l \\ m_2 m_l}}(\omega, z, \delta) \otimes \Omega_{\substack{m_l m_1 \\ m_l m_2}}(\omega, z) - cc\right] + i\left[\rho_{\substack{m_2 m_l \\ m_1 m_l}}(\omega, z, \delta) \otimes \Omega_{\substack{m_l m_2 \\ m_l m_1}}(\omega, z) - cc\right] \\
- \Gamma_l \rho_{m_l m_l}(\omega, z, \delta) + \Gamma_{\frac{1}{2}} \rho_{\substack{m_1 m_1 \\ m_2 m_2}}(\omega, z, \delta).
\end{aligned}
\tag{18}
$$

By substituting Eqs. (12) and (13) into Eq. (18), it can be deduced that (cc is the abbreviation for complex conjugated quantity)

$$\rho_{m_l m_l}(\omega,z,\delta) - \rho_{\substack{m_1 m_1 \\ m_2 m_2}}(\omega,z,\delta) = i\, \frac{2\rho_{\substack{m_1 m_l \\ m_2 m_l}}(\omega,z,\delta) \otimes \Omega_{\substack{m_1 m_1 \\ m_1 m_2}}(\omega,z) + \rho_{\substack{m_2 m_l \\ m_1 m_l}}(\omega,z,\delta) \otimes \Omega_{\substack{m_l m_2 \\ m_l m_1}}(\omega,z) - cc}{i\omega + \Gamma_{ul}}$$

$$- \frac{\delta_{ul}}{i\omega + \Gamma_{ul}}\left[\rho_{m_l m_l}(\omega,z,\delta) + \rho_{\substack{m_1 m_1 \\ m_2 m_2}}(\omega,z,\delta)\right] + \frac{\Lambda_l(\omega,z,\delta) - \Lambda_{\frac{1}{2}}(\omega,z,\delta)}{i\omega + \Gamma_{ul}}. \tag{19}$$

Similarly, by summing up Eq. (4) and Eq. (5), it becomes

$$\rho_{m_l m_l}(\omega,z,\delta) + \rho_{\substack{m_1 m_1 \\ m_2 m_2}}(\omega,z,\delta) = i\, \frac{\rho_{\substack{m_2 m_l \\ m_1 m_l}}(\omega,z,\delta) \otimes \Omega_{\substack{m_l m_2 \\ m_l m_1}}(\omega,z) - cc}{i\omega + \Gamma_{ul}} - \frac{\delta_{ul}}{i\omega + \Gamma_{ul}}\left[\rho_{m_l m_l}(\omega,z,\delta) - \rho_{\substack{m_1 m_1 \\ m_2 m_2}}(\omega,z,\delta)\right]$$

$$+ \frac{\Lambda_l(\omega,z,\delta) + \Lambda_{\frac{1}{2}}(\omega,z,\delta)}{i\omega + \Gamma_{ul}}. \tag{20}$$

C. Modeling the electromagnetic field

We are examining the case of molecules probed by an EM field "trapped" inside a high-finesse cavity with a characteristic time that can exceed 150 μs and an accurately selected TEM$_{00}$ spatial mode (rejection rate $> 100{:}1$). The time scale relative to the variation of the envelope of the EM field is a lot longer than that relative to any other relaxation processes involved in the absorption process. Hence it becomes relevant to consider a monochromatic EM field. This inclines us to look for a solution of the equations by inserting the Rabi frequency,

$$\Omega_{m_u m_l}(\omega,z) = 2\pi \Omega_{m_u m_l}^{(0)}[\delta(\omega - \omega_0) + \delta(\omega + \omega_0)]\cos(kz)$$
$$= \Omega_{m_l m_u}^*(\omega,z), \tag{21}$$

where $\Omega_{m_u m_l}^{(0)} = |\mu_{m_u m_l}|E_0/\hbar$ and ω_0 is the carrier angular frequency of the probing EM field in the laboratory frame (k is the wave vector). The amplitude and the polarization direction of both counter-propagating EM fields (forming a standing wave) are assumed to be identical. In addition, an optically thin absorbing medium is assumed ($\alpha L_{eq} \ll 1$, L_{eq} is the equivalent absorption length and α is the absorption coefficient; see Sec. II E). Thus, the amplitude of the EM field is only barely altered by the absorption process.

The Rabi frequency given by Eq. (21) requires further comment because it ignores the effective shape of the field experienced by molecules traveling across a cylinder-shaped EM radiation. Assuming a uniform transverse velocity v_x, the cylindricity of the Gaussian EM field demands consideration of a Gaussian shape for the Rabi frequency $\Omega_{m_u m_l}(\omega,z)$, whose frequency extension is governed by the transit time. It turns out that, for molecules traveling at $v_y = 0$, the Dirac δ function of Eq. (21) should be replaced by a Gaussian function with an HWHM frequency extension,

$$\Delta_\omega = \frac{2\sqrt{\ln(2)}}{w_0/v_x}, \tag{22}$$

where w_0 is the TEM$_{00}$ cavity mode beam waist radius (or minimum spot size [59]). Furthermore, the de facto dispersion of the component v_y of the speed ($\overline{v_y} = 0$), due to the poor planarity of the expansion (V shaped), provides a frequency extension distribution with a lower limit given by Eq. (22).

To overcome the difficulty of solving the system of equations without analytical integral expression when plugging in an effective Gaussian EM field, we opted to keep the Rabi frequency as provided by Eq. (21) and to assume that the transit time controls the population relaxation rates (it is discussed in Secs. VII B and VIII). This supposes that a Gaussian shape can be approached by an exponential decay when both functions have the same FWHM. For $v_y = 0$, this can be obtained by setting

$$\Gamma_u = \Gamma_l = \frac{v_x}{w_0}\sqrt{\frac{\ln(2)}{2}}. \tag{23}$$

In the framework of this assumption the radiative processes (cf. the laser-induced fluorescence), which could contribute to the relaxation of the upper state, are ignored. Despite the lack of reported data for NO$_2$ species in the energy range of interest, reasonable extrapolations indicate that the radiative lifetime should be longer than 100 μs in the absence of collisions [60]. Even if the role of collisions cannot be totally excluded in the jet expansion [61,62], they should not significantly alter the radiative lifetime.

D. Population saturation

The use of a continuous jet expansion allows the allotment of a time-independent source of molecules characterized by a velocity distribution driving the source terms,

$$\Lambda_i(\omega,z,\delta) = 2\pi \Lambda_i^{(0)} g_\Delta(\delta)\,\delta(\omega), \tag{24}$$

where $\Lambda_i^{(0)}$ ($i = l$ or u) are constant quantities for the specified level and where $g_\Delta(\delta)$ is a normalized function with a velocity extension Δ/k following

$$\int_{-\infty}^{\infty} g_\Delta(\delta)\,d\delta = 1. \tag{25}$$

To deal with molecules capable of absorbing EM radiations at two different frequencies (dual absorption), when they travel with a velocity projection $v_z \neq 0$, the total population is assumed to be the sum of two distinct populations:

$$\rho_{m_l m_u}(\omega,z,\delta) = \rho_{m_l m_u}^{(-)}(\omega,z,\delta) + \rho_{m_l m_u}^{(+)}(\omega,z,\delta). \tag{26}$$

Theoretically the case $\delta = 0$ should be treated separately because molecules without Doppler shift may interact specifically with the EM field since they barely cross the interference pattern. However, we consider that the number of molecules exhibiting such a speed is small;

hence they almost do not contribute to the observed RD signal.

Convoluting Eq. (17) by the Rabi frequency, (21) (see Appendix B), and then eliminating the nonresonant terms (RWA), it becomes

$$\rho_{m_l m_u}^{(\pm)}(\omega, z, \delta) \otimes \Omega_{m_u m_l}(\omega, z) = \Omega_{m_u m_l}^{(0)^2} \frac{\cos^2(kz)}{2} \left[\frac{\rho_{m_l m_l}(\omega, z, \delta) - \rho_{m_u m_u}(\omega, z, \delta)}{\omega_{ul} - \omega - \omega_0 \pm \delta + i\gamma_{ul}} + \frac{\rho_{m_l m_l}(\omega - 2\omega_0, z, \delta) - \rho_{m_u m_u}(\omega - 2\omega_0, z, \delta)}{\omega_{ul} - \omega + \omega_0 \pm \delta + i\gamma_{ul}} \right]. \tag{27}$$

The convolution of the coherence terms clearly shows two spectral extensions controlled by the population inversions: one frequency unshifted and one shifted around $2\omega_0$ (and $-2\omega_0$ for the complex conjugated term). None of them should be ignored in a full treatment. Here, we assume that the extensions at twice the carrier frequency are small and the harmonic frequency development is truncated at the lowest order.

Focusing on the stationary (steady-state) solutions, only the frequency components of the density matrix at $\omega = 0$ need to be calculated. Nevertheless, the behavior for any time can be obtained by considering all the low frequencies ($\omega \neq 0$) and by inverse Fourier transforming.

Combining Eqs. (26) and (27), we get

$$\rho_{m_l m_u}(0, z, \delta) \otimes \Omega_{m_u m_l}(0, z) - cc$$
$$= -i \frac{\Omega_{m_u m_l}^{(0)^2} \cos^2(kz)}{\gamma_{ul}} \left[\rho_{m_l m_l}(0, z, \delta) - \rho_{m_u m_u}(0, z, \delta) \right]$$
$$\times \left[\mathcal{L}_u^{(+)} + \mathcal{L}_u^{(-)} \right], \tag{28}$$

where

$$\mathcal{L}_u^{(\pm)} = \frac{\gamma_{ul}^2}{(\omega_{ul} - \omega_0 \pm \delta)^2 + \gamma_{ul}^2}. \tag{29}$$

Using the longitudinal relaxation time,

$$T_1 = \frac{1}{2\Gamma_u} + \frac{1}{2\Gamma_l} = \frac{\Gamma_{ul}}{\Gamma_{ul}^2 - \delta_{ul}^2}, \tag{30}$$

and substituting Eq. (20) into Eq. (19), it is easy to show that

$$\left[1 + \hat{s}_{m_1 m_l} + \frac{\Gamma_{uu}}{2\Gamma_{ul}} \hat{s}_{m_2 m_l} \right] \rho_{ll}(0, z, \delta)$$
$$- (1 + \hat{s}_{m_1 m_l}) \rho_{11}(0, z, \delta) - \frac{\Gamma_{uu}}{2\Gamma_{ul}} \hat{s}_{m_2 m_l} \rho_{22}(0, z, \delta)$$
$$= 2\pi \delta(\omega) \left[\frac{\Lambda_{ll}^{(0)}}{\Gamma_{ll}} - \frac{\Lambda_{11}^{(0)}}{\Gamma_{uu}} \right] g_\Delta(\delta), \tag{31}$$

where the so-called saturation coefficient $\hat{s}_{m_u m_l}$ is defined by

$$\hat{s}_{m_u m_l} = 2 \Omega_{m_u m_l}^{(0)^2} \cos^2(kz) \frac{T_1}{\gamma_{ul}} \left[\mathcal{L}_u^{(+)} + \mathcal{L}_u^{(-)} \right]. \tag{32}$$

An additional equation can be readily derived by permuting both index 1 and index 2 in Eq. (31).

Finally, combining Eqs. (10) and (11), we get

$$[1 + \hat{s}_{m_1 m_l} + \hat{s}_{m_2 m_l}] \rho_{m_l m_l}(0, z, \delta) - (1 + \hat{s}_{m_1 m_l}) \rho_{m_1 m_1}(0, z, \delta)$$
$$- (1 + \hat{s}_{m_2 m_l}) \rho_{m_2 m_2}(0, z, \delta)$$
$$= 2\pi \left[\frac{\Lambda_l^{(0)}}{\Gamma_{ll}} - \frac{\Lambda_1^{(0)}}{\Gamma_{uu}} - \frac{\Lambda_2^{(0)}}{\Gamma_{uu}} \right] \delta(\omega) g_\Delta(\delta). \tag{33}$$

Equations (31) and (33) shape a linear system of three equations which can be solved easily. Setting $\frac{\Lambda_1^{(0)}}{\Gamma_u} = \frac{\Lambda_2^{(0)}}{\Gamma_u} = \mathcal{N}_0 e^{-\frac{E_u}{kT}}$ and $\frac{\Lambda_l^{(0)}}{\Gamma_{ll}} = \mathcal{N}_0 e^{-\frac{E_l}{kT}}$ (T is the temperature characterizing the Maxwell-Boltzmann distribution and $\mathcal{N}_0$ is the number density of molecules),[1] it becomes

$$\rho_{m_l m_l}(0, z, \delta) - \rho_{\substack{m_1 m_1 \\ m_2 m_2}}(0, z, \delta)$$
$$= 2\pi \delta(\omega) \frac{\mathcal{N}_0 g_\Delta(\delta) \left[1 + \hat{s}_{\substack{m_2 m_2 \\ m_1 m_1} m_l}(1 - \beta) \right] \left[e^{-\frac{E_l}{kT}} - e^{-\frac{E_u}{kT}} \right]}{1 + \hat{s}_{m_1 m_l} + \hat{s}_{m_2 l_l} + \hat{s}_{m_1 m_l} \hat{s}_{m_2 m_l}(1 - \beta^2)}, \tag{34}$$

where

$$\beta = \frac{\Gamma_{uu}}{2\Gamma_{ul}}. \tag{35}$$

E. Nonlinear absorption coefficient

The absorption coefficient can be obtained by calculating the macroscopic scalar polarization. Keeping the monochromatic EM field assumption, the macroscopic polarization (specific to a frequency detuning) for the steady-state solution becomes (ϵ_0 is the vacuum permittivity)

$$P(\omega, z, \delta) = \epsilon_0 \chi_{ul}(\omega, z, \delta) \otimes E(\omega, z) = \text{Tr}(\rho.\mu)$$
$$= \sum_{m_u} \sum_{m_l} \rho_{m_l m_u}(0, z, \delta) \mu_{m_u m_l}, \tag{36}$$

where (see Sec. II C)

$$E(\omega, z) = 2\pi E_0 [\delta(\omega - \omega_0) + \delta(\omega + \omega_0)] \cos(kz). \tag{37}$$

----

[1]Jet expansions are environments which cannot be characterized by a unique temperature; this point is discussed in Sec. VII C 1.

The absence of direct coupling between the two upper levels ($\mu_{12} = 0$) cancels out the straight contributions to the trace operator (Tr), which could result from nonvanishing cross-coherence terms. Attentive scrutiny shows that the scalar nonlinear susceptibility $\chi_{ul}(\omega,z,\delta)$ exhibits a quadratic dependence on the amplitude of the EM field.

The coherence density-matrix elements are obtained by inserting Eq. (34) into Eq. (17). The steady-state frequency detuning specific nonlinear absorption coefficient of the $u \leftrightarrow g$ transition is obtained from the imaginary part (Im) of

the nonlinear susceptibility; then by summing up the three components of the polarization vector,

$$\alpha_{ul}(\omega_0,z,\delta) = \frac{\omega_0}{c} \operatorname{Im}(\chi_{ul}(\omega_0,z,\delta))$$

$$= 3 \sum_{m_u} \sum_{m_l} \alpha_{m_u m_l}(\omega_0,z,\delta). \qquad (38)$$

It finally follows for the three-level system previously described that

$$\alpha_{m_u m_l}(\omega_0,z,\delta) = \frac{\pi \omega_0}{3\epsilon_0 \hbar c} \frac{\mathcal{N}_0 \, g_\Delta(\delta)}{Q} g_{\text{ns}}$$

$$\times \frac{\left[e^{-\frac{E_l}{kT}} - e^{-\frac{E_1}{kT}}\right][1+\hat{s}_{m_2 m_l}(1-\beta)]\left[\mathcal{L}_1^{(+)} + \mathcal{L}_1^{(-)}\right]\frac{\mu_{m_1 m_l}^2}{\gamma_{1l}} + \left[e^{-\frac{E_l}{kT}} - e^{-\frac{E_2}{kT}}\right][1+\hat{s}_{m_1 m_l}(1-\beta)]\left[\mathcal{L}_2^{(+)} + \mathcal{L}_2^{(-)}\right]\frac{\mu_{m_2 m_l}^2}{\gamma_{2l}}}{1 + \hat{s}_{m_1 m_l} + \hat{s}_{m_2 m_l} + (1-\beta^2)\hat{s}_{m_1 m_l}\hat{s}_{m_2 m_l}}$$

$$= \frac{\sum_{u=1}^{2} \alpha_{m_u m_l}^{(0)'}(\omega_0,z,\delta)}{1 + \hat{s}_{m_1 m_l} + \hat{s}_{m_2 m_l} + (1-\beta^2)\hat{s}_{m_1 m_l}\hat{s}_{m_2 m_l}}, \qquad (39)$$

where E_i are the energies of the levels involved in the transitions ($\hbar\omega_{ul} = E_u - E_l$), Q is the partition function,

$$Q = \sum_X \sum_m e^{-\frac{E_m}{kT}} = \sum_X d_X e^{-\frac{E_X}{kT}}, \qquad (40)$$

$d_X = g_{\text{ns}}(2X+1)$, g_{ns} is the nuclear spin statistic, and

$$\alpha_{m_u m_l}^{(0)'}(\omega_0,z,\delta) = \alpha_{m_u m_l}^{(0)}(\omega_0,z,\delta)\left[1 + \hat{s}_{m_{u'} \neq m_u m_l}(1-\beta)\right], \qquad (41)$$

where

$$\alpha_{m_u m_l}^{(0)}(\omega_0,z,\delta) = \frac{\pi\omega_0}{3\epsilon_0 \hbar c} g_{\text{ns}} \frac{e^{-\frac{E_l}{kT}} - e^{-\frac{E_u}{kT}}}{Q}\left[\mathcal{L}_u^{(+)} + \mathcal{L}_u^{(-)}\right]$$

$$\times \frac{\mu_{m_u m_l}^2}{\gamma_{1u}} \mathcal{N}_0 \, g_\Delta(\delta) \qquad (42)$$

is the linear absorption associated with the subtransition.

Of course, the linear absorption coefficient of a three-level system can be readily derived by setting $\hat{s}_{m_u m_l} = 0$ in Eq. (39). It is the anticipated sum of the two absorption coefficients $\alpha_{m_1 m_l}^{(0)}(\omega_0,z,\delta)$ and $\alpha_{m_2 m_l}^{(0)}(\omega_0,z,\delta)$.

It is noteworthy that the denominator of Eq. (39) raises three (narrow) "resonant" terms since it exhibits maxima at $\omega_0 = \omega_{ul} \pm \delta$ and $\omega_0 = \frac{\omega_1 + \omega_2}{2}$. After integration, the "resonances" at $\omega_0 \simeq \omega_{ul}$ provide the "usual" saturation dip (or Lamb hole [2]) characterizing the SA transitions, while the resonance at $\omega_0 \simeq \frac{\omega_1 + \omega_2}{2}$ provides the so-called "crossover" dip at the mean frequency of the two "usual" transitions.

F. Multi-Zeeman sublevel absorption

The formalism established in Sec. II E can be extended to a multiple-line interfering absorption pattern (i.e., for a number of interfering lines greater than two). For n transitions in a "V" shape configuration the denominator of Eq. (39) becomes

$$1 + \sum_{i=0}^{n-1}(1-\beta)^i \, (1+i\beta) \sum_{j=0}^{C_{i+1}^{n-1}} \prod_{k=j}^{i+j} \hat{s}_{m_{k\%n} m_l}, \qquad (43)$$

where $\%$ denotes the function modulo and $C_i^j = \frac{j!}{i!(j-i)!}$, whereas its numerator becomes

$$\frac{\pi\omega_0}{3\epsilon_0 \hbar c} \frac{\mathcal{N}_0 \, g_\Delta(\delta) \, g_{\text{ns}}}{Q} \times \sum_u \left[1 + \sum_{i=1}^{n-1}(1-\beta)^i \sum_{j=0}^{C_{i-1}^n} \prod_{k=j, k\neq u}^{i+j-1} \hat{s}_{m_{k\%n} m_l}\right]\left[\mathcal{L}_u^{(+)} + \mathcal{L}_u^{(-)}\right]\frac{\mu_{m_u m_l}^2}{\gamma_{lu}}\left[e^{-\frac{E_l}{kT}} - e^{-\frac{E_u}{kT}}\right]. \qquad (44)$$

For a "Λ" shape configuration, the indices u and l need to be permuted.

As mentioned in Sec. II A, in the absence of Zeeman sublevel degeneracy lift, the $u \longleftarrow g$ transition absorption results from the absorption of each subtransition as given

by Eq. (38). The polarization vector of the applied EM field controls the optical selection rules between the Zeeman components. A linearly polarized EM field is assumed for the rest of the study (the molecular orientation is then conserved). It follows for the squared molecular dipole moment of the

subtransition (or sub–line strength), after applying the Wigner-Eckart theorem [63], that

$$
\begin{aligned}
\mu^2_{m_u m_l} &= |\langle u X_u \kappa_u m_u | \vec{\mu} \cdot \hat{\epsilon}^* | l X_l \kappa_l m_l \rangle|^2 \\
&= \begin{pmatrix} X_u & 1 & X_l \\ m_u & 0 & -m_l \end{pmatrix}^2 |\langle u X_u \kappa_u \| \vec{\mu} \| l X_l \kappa_l \rangle|^2 \\
&= \begin{pmatrix} X_u & 1 & X_l \\ m_u & 0 & -m_l \end{pmatrix}^2 \mathcal{S}^u_l \mu^2_{\text{band}} = \mu^2_{ul_m},
\end{aligned}
\tag{45}
$$

where $\mathcal{S}^u_l \mu^2_{\text{band}}$ is the usual line strength (μ^2_{band} being the band strength), $\hat{\epsilon}$ denotes the direction of the EM field in the space-fixed frame, and "." denotes the scalar or dot product). Interferences between transitions belonging to different bands are ignored here. The value of the factor $\mathcal{S}^u_l$ is given by the eigenvectors of the molecular Hamiltonian (see Sec. IV, e.g.).

The insertion of Eq. (45) into Eq. (39) shows how the sub–line strengths contribute to the total line strength; the Wigner 3j coefficient alters not only the "linear" absorption factor [embedded in the numerator of Eq. (39)] but also the Rabi frequency,

$$
\Omega^2_{m_u m_l} = \begin{pmatrix} X_u & 1 & X_l \\ m_u & 0 & -m_l \end{pmatrix}^2 \Omega^{(0)^2}_{ul}.
\tag{46}
$$

Hence the saturation parameter $\hat{s}_{m_u m_l}$ can be defined as

$$
\hat{s}_{m_u m_l} = \begin{pmatrix} X_u & 1 & X_l \\ m_u & 0 & -m_l \end{pmatrix}^2 \times \hat{s}_{ul} = \begin{pmatrix} X_u & 1 & X_l \\ m_u & 0 & -m_l \end{pmatrix}^2 \mathcal{S}^u_l s^{(0)}_{ul},
\tag{47}
$$

where

$$
s^{(0)}_{ul} = 2 \frac{\mu^2_{\text{band}} E^2_0}{\hbar^2} \cos^2(kz) \frac{T_1}{\gamma_{ul}} \left[\mathcal{L}^{(+)}_u + \mathcal{L}^{(-)}_u \right].
\tag{48}
$$

It is worth pointing out that the double sum in Eq. (38) can be replaced by a single sum since only the linear polarization of the EM field is considered here. We deduce that only subtransitions sharing a same value of m (i.e., $m_1 = m_2 = m_l$) can interfere.

G. Total absorption

The transverse dependence of the EM field probing the molecules has been mentioned in Sec. II C (mode TEM$_{00}$). A spatial modulation along the z axis strengthens this transverse dependence of the EM field. The hyperbolic variation of the EM-field amplitude along the z axis can be ignored because

the jet expansion is located at the center of the cavity and the absorption path is small. With respect to these spatial behaviors two limit cases can be established: (i) the molecule population follows the spatial modulation adiabatically and the z and $\sqrt{x^2 + y^2}$ dependencies need to be included in the saturation parameter, which requires calculation of the relevant integrals; and (ii) the population does not follow spatial EM-field changes like those due to the interference pattern of the counter-propagating beams and no spatial integration is required. In the second case the molecules travel through an average standing wave and we can set $\langle \cos^2(kz) \rangle = 1/2$. This is discussed later (see Sec. VII B).

The velocity dependence can easily be taken into account by assuming a Maxwell-Boltzmann distribution of the molecular speed:

$$
g_\Delta(\delta) = \sqrt{\frac{\ln 2}{\pi}} \frac{1}{\Delta_D} e^{-\ln 2 \left(\frac{\delta}{\Delta_D} \right)^2}.
\tag{49}
$$

The total absorption coefficient is obtained by integrating the absorption coefficients [given by Eq. (38)]:

$$
\alpha_{ul}(\omega_0, z) = \int_0^\infty \alpha_{ul}(\omega_0, z, \delta) \, d\delta.
\tag{50}
$$

Unfortunately, no analytical integral form of Eq. (39) can be derived when substituting in the distribution as given by Eq. (49), therefore numerical integrations are performed. However, analytical forms can be derived with regard to some specific cases. For example, an integral expression of the absorption can be inferred for a two-level system. Naturally, the latter case is inappropriate for simulation of crossover resonances.

1. Saturated absorption due to a single transition

Equation (39) can be analytically integrated when only one transition is considered (setting $u = 1$) by using the plasma dispersion function [64] (or werf). It gives

$$
\begin{aligned}
&\alpha_{m_u m_l}(\omega_0, z) \\
&= \frac{\pi \omega_0}{3 \epsilon_0 \hbar c} \frac{e^{-\frac{E_l}{kT}} - e^{-\frac{E_u}{kT}}}{Q} g_{\text{ns}} \mu^2_{\text{band}} \mathcal{S}^u_l \\
&\quad \times \begin{pmatrix} X_u & 1 & X_l \\ m_u & 0 & -m_l \end{pmatrix}^2 \mathcal{N}_0 \, \mathcal{G}_{\text{NL}}(\omega_{ul} - \omega_0, z),
\end{aligned}
\tag{51}
$$

where

$$
\begin{aligned}
\mathcal{G}_{\text{NL}}(\omega, z) = {}& \frac{1}{\Delta_D} \frac{2\sqrt{\pi \ln 2}}{\left[\left(\frac{\Omega_+(z)}{\gamma_{ul}} \right)^2 - \left(\frac{\Omega_-(z)}{\gamma_{ul}} \right)^2 \right]} \left[\frac{1 + \left(\frac{\Omega}{\gamma_{ul}} \right)^2 - \left[\frac{\Omega_-(\Omega,z)}{\gamma_{ul}} \right]^2}{\frac{\Omega_-(\Omega,z)}{\gamma_{ul}}} \text{werf} \left(\frac{i\Omega_-(\Omega,z)}{\Delta_D / \sqrt{\ln 2}} \right) \right. \\
&\left. - \frac{1 + \left(\frac{\Omega}{\gamma_{ul}} \right)^2 - \left[\frac{\Omega_+(\Omega,z)}{\gamma_{ul}} \right]^2}{\frac{\Omega_+(\Omega,z)}{\gamma_{ul}}} \text{werf} \left(\frac{i\Omega_+(\Omega,z)}{\Delta_D / \sqrt{\ln 2}} \right) \right]
\end{aligned}
\tag{52}
$$

is a nonlinear line profile and where $\Omega_+(z)$ and $\Omega_-(z)$ are two conjugated quantities if both are complex quantities, defined by

$$\left[\frac{\Omega_\pm(\Omega,z)}{\gamma_{ul}}\right]^2 = 1 + s_{m_u m_l} - \left(\frac{\Omega}{\gamma_{ul}}\right)^2$$
$$\pm \sqrt{s_{m_u m_l}^2 - 4\left(1 + s_{m_u m_l}\right)\left(\frac{\Omega}{\gamma_{ul}}\right)^2}, \quad (53)$$

where

$$s_{m_u m_l} = 2\frac{\mu_{m_u m_l}^2 E_0^2}{\hbar^2} \cos^2(kz) \frac{T_1}{\gamma_{ul}}. \quad (54)$$

Both quantities inside the brackets in the numerator of Eq. (52) are also conjugated if $\Omega_+(z)$ and $\Omega_-(z)$ are both complex conjugated quantities. A similar expression can be found in Ref. [65]. If the coherence relaxation rate γ_{ul} is low compared with the Doppler broadening, the function werf can be approximated by a Gaussian profile as given in Ref. [66] (the so-called crude approximation). If $s_{m_u m_l} = 0$, the nonlinear line profile $\mathcal{G}_{\text{NL}}(\omega,z)$ becomes the usual Voigt profile.

Also, let us note that an expression similar to Eq. (39) (for a single transition) was obtained by Haroche and Hartmann [45] for the case of a pump-probe scheme: they omitted the double sums $\mathcal{L}_u^{(+)} + \mathcal{L}_u^{(-)}$ ($u = 1$ or 2) and replaced them with unique Lorentzian profiles. However, they obtained an additional contribution to the development because they extended their calculations to a higher order.

2. An alternative approximation for noninterfering transitions

Analysis of Eq. (39) shows that the amplitude of the resonances are mainly controlled by the terms $\mathcal{L}_u^{(+)} + \mathcal{L}_u^{(-)}$ sitting in its denominator. In the case of dual interference, the sum formed by the two terms $\mathcal{L}_1^{(+)} + \mathcal{L}_1^{(-)}$ and $\mathcal{L}_2^{(+)} + \mathcal{L}_2^{(-)}$ becomes maximum, and equal to 2, at $\omega_0 = \omega_{1l} \pm \delta$, $\omega_0 = \omega_{2l} \pm \delta$, or $\omega_0 = (\omega_1 + \omega_2)/2$, which gives rise to the three dips previously obtained after the integration over δ. If the two transitions do not share a same level (two independent two-level systems), no interference can appear and the absorption coefficient $\alpha_{m_u m_l}(\omega_0, z, \delta)$ is provided by

$$\frac{\pi\omega_0}{3\epsilon_0\hbar c} \frac{\mathcal{N}_0 \, g_\Delta(\delta)}{Q} \times \frac{g_{\text{ns}_1}\left[e^{-\frac{E_l}{kT}} - e^{-\frac{E_1}{kT}}\right]\left[\mathcal{L}_1^{(+)} + \mathcal{L}_1^{(-)}\right]\frac{\mu_{1m_l}^2}{\gamma_{1l}} + g_{\text{ns}_2}\left[e^{-\frac{E_l}{kT}} - e^{-\frac{E_2}{kT}}\right]\left[\mathcal{L}_2^{(+)} + \mathcal{L}_2^{(-)}\right]\frac{\mu_{2m_l}^2}{\gamma_{2l}}}{1 + s_{m_1 m_l}\left[\mathcal{L}_1^{(+)} + \mathcal{L}_1^{(-)}\right] + s_{m_2 m_l}\left[\mathcal{L}_2^{(+)} + \mathcal{L}_2^{(-)}\right]}. \quad (55)$$

This expression offers the great advantage of being analytically integrable over the spatial coordinates z and $\sqrt{x^2 + y^2}$ for a Gaussian EM field. After careful inspection it can be seen that this integral exhibits (i) a global behavior very similar to that obtained when the transitions interfere, (ii) the correct behavior around the dips at $\omega_0 = \omega_1$ and $\omega_0 = \omega_2$, and (iii) incorrect behavior near the crossover dip the amplitude of the crossover resonance is twice as high as that expected for interfering transitions. In fact, Eq. (55) can be deduced readily from the density-matrix formalism by considering two decoupled two-level systems.

III. THE MOLECULAR HAMILTONIAN

NO$_2$ is a radical species ($S = 1/2$, $\boldsymbol{S}$ is the electronic-spin angular momentum) exhibiting a high symmetry (C_{2v} [67]) and a rigid frame in first approximation. Given the null nuclear spin of the permutable oxygen atoms (^{16}O) and the nuclear spin of the most abundant isotopic nitrogen atom (^{14}N), 1, the nuclear spin statistic weight can be deduced for each vibronic level by using the usual symmetry-group properties [51]. For a ground vibronic level of symmetry, A_1, it becomes $g_{\text{ns}} = 0$ if $K_a + K_c$ is odd and $g_{\text{ns}} = 3$ if $K_a + K_c$ is even; and for an upper state of symmetry, it is B_2, $g_{\text{ns}} = 3$ if $K_a + K_c$ is odd and $g_{\text{ns}} = 0$ if $K_a + K_c$ is even.

The total nuclear spin is $I = 1$, which requires us to deal with the hyperfine Hamiltonian in addition to the spin-rotation Hamiltonian. We assume that a J-scheme of coupling [53] applies: $\boldsymbol{F} = \boldsymbol{J} + \boldsymbol{I}$ ($\boldsymbol{F}$ is the total molecular angular momentum), $\boldsymbol{J} = \boldsymbol{N} + \boldsymbol{S}$ ($\boldsymbol{N}$ is the rotational angular momentum). The effective molecular Hamiltonian is

$$\mathcal{H} = \mathcal{H}_{\text{rot}} + \mathcal{H}_{\text{SR}} + \mathcal{H}_{\text{hf}}, \quad (56)$$

where $\mathcal{H}_{\text{rot}}$ can be cast in Cartesian coordinates attached to the principal axis system (using the I^r representation [68]),

$$\mathcal{H}_{\text{rot}} = AN_a^2 + BN_b^2 + CN_c^2, \quad (57)$$

where A, B, and C are the usual rotational constants associated with the respective a, b, and c principal axes of inertia. $\mathcal{H}_{\text{SR}}$ is yielded by

$$\mathcal{H}_{\text{SR}} = \tfrac{1}{2}(\boldsymbol{N}\boldsymbol{\epsilon}\boldsymbol{S} + \boldsymbol{S}\boldsymbol{\epsilon}\boldsymbol{N}), \quad (58)$$

where $\boldsymbol{\epsilon}$ is the quadratic spin-rotation tensor [69], and $\mathcal{H}_{\text{hf}}$ is

$$\mathcal{H}_{\text{hf}} = \mathcal{H}_{\text{FC}} + \mathcal{H}_{\text{dip}}, \quad (59)$$

where

$$\mathcal{H}_{\text{FC}} = a_{\text{FC}} \, \boldsymbol{I} \cdot \boldsymbol{S}, \quad (60)$$

is the Fermi contact interaction and

$$\mathcal{H}_{\text{dip}} = -g_S g_I \mu_B \mu_N \left[\frac{\boldsymbol{I} \cdot \boldsymbol{S}}{r^3} - \frac{3(\boldsymbol{I} \cdot \boldsymbol{r})(\boldsymbol{S} \cdot \boldsymbol{r})}{r^5}\right]$$
$$= \boldsymbol{I} \cdot \boldsymbol{T}(r) \cdot \boldsymbol{S} \quad (61)$$

describes the electronic-spin nuclear-spin dipole interaction. g_S is the free-spin g factor, g_I is the nuclear Landé factor,

TABLE I. Molecular Hamiltonians with operators in cylindrical coordinates and associated selection rules ($\Delta F = 0$).

	$\Delta K = 0$	$\Delta K = \pm 2$	ΔN	ΔJ
$\mathcal{H}_{\rm rot}$	$(\frac{B+C}{2})\boldsymbol{N}^2 + (A - \frac{B+C}{2})\boldsymbol{N}_a^2$	$\frac{B-C}{4}(\boldsymbol{N}_+^2 + \boldsymbol{N}_-^2)$	0	0
$\mathcal{H}_{\rm SR}$	$(\frac{\tilde{\epsilon}_{bb}+\tilde{\epsilon}_{cc}}{2})\boldsymbol{N}\cdot\boldsymbol{S} + (\tilde{\epsilon}_{aa} - \frac{\tilde{\epsilon}_{bb}-\tilde{\epsilon}_{cc}}{2})\boldsymbol{N}_a^2\frac{\boldsymbol{N}\cdot\boldsymbol{S}}{N^2}$	$\frac{\tilde{\epsilon}_{bb}-\tilde{\epsilon}_{cc}}{4}(\boldsymbol{N}_+^2 + \boldsymbol{N}_-^2)\frac{\boldsymbol{N}\cdot\boldsymbol{S}}{N^2}$	$0, \pm 1$	0
$\mathcal{H}_{\rm FC}$	$a_{\rm FC}\boldsymbol{S}\cdot\boldsymbol{I}$	0	0	$0, \pm 1$
$\mathcal{H}_{\rm dip}$	$\frac{T_{aa}}{2}(\boldsymbol{S}\cdot\boldsymbol{I} - 3\boldsymbol{S}_a\boldsymbol{I}_a)$	$(\frac{T_{aa}}{2} + \frac{T_{bb}}{4})(\boldsymbol{I}_+\boldsymbol{S}_+ + \boldsymbol{I}_-\boldsymbol{S}_-)$	$0, \pm 1$	$0, \pm 1$

μ_B and μ_N are the Bohr and nuclear magnetons, respectively [53], and $\boldsymbol{T}(r)$ is the second-order electronic-spin nuclear-spin dipole tensor [70].

Ignoring the Zeeman components temporally, the matrix elements of $\mathcal{H}$ can be calculated in the basis set adapted to a J-scheme of coupling [71], $|\psi_{\rm ev}SJIF\,NK\rangle = |\psi_{\rm ev}\rangle\,|NK\rangle\,|S\rangle\,|I\rangle$, where $|N\,K\rangle$ are the eigenvectors of the symmetric top rotational Hamiltonian ($-N \leqslant K \leqslant N$). The expression of the matrix elements of each Hamiltonian is available in the literature [52,53,71–73]. Nevertheless, the expression of the Hamiltonian terms in cylindrical coordinates, as well as the associated selection rules, are listed in Table I, using the usual reduced spin-rotation Hamiltonian [69].

IV. MODIFIED WANG SYMMETRY AND LINE STRENGTH

The high (orthorhombic) symmetry of NO_2 radical enables the $\Delta K = \pm 1$ matrix elements to be washed out. In addition, the matrix elements satisfy the K-sign exchange property ($\Delta N = N' - N$, $\Delta K = K' - K = 0, \pm 2$),

$$\langle S\,J\,I\,F\,N\,K|\mathcal{H}|S\,J'\,I\,F\,N'\,K'\rangle$$
$$= (-1)^{\Delta N}\,\langle S\,J\,I\,F\,N - K|\mathcal{H}|S\,J'\,I\,F\,N' - K'\rangle, \quad (62)$$

where $\mathcal{H}$ is defined by Eq. (56) and its embedded terms (see Sec. III).

Similarly to the unitary Wang transformation regarding the rotational Hamiltonian which gives the four symmetries $O_\pm/E_\pm$ [74], spin-rotation Wang symmetry (SRWS) can be established [52,75]. Unfortunately, the $\Delta J = \pm 1$ matrix elements of the hyperfine Hamiltonian mix the SRWS. Never-

theless, hyperfine-spin-rotation Wang symmetry (HFWS) can be provided by using a specific modified Wang transformation. Despite the similar notation, the HFWS denoted Sy here ($Sy = \pm$, following Raynes [75]; the labels 1 and 2 might be preferred to $\pm$) should not be confused with the usual Wang symmetry associated with the pure (eventually distorted) rotational Hamiltonian.

After diagonalization of the molecular Hamiltonian matrix of full size, $[(2F + 1)(2I + 1)(2S + 1)]^2$ (it can be blocked into four submatrices by applying the modified Wang transformation previously mentioned) for each vibronic level (i.e., l and u). Dealing now with a specific molecular Hamiltonian, the generic eigenvectors can be replaced by the relevant hyperfine eigenvectors as follows (in a nonsymmetrized basis set):

$$|SI \pm F\tau\rangle = \sum_{J=|F-I|}^{F+I}\sum_{N=|J-S|}^{J+S}\sum_{K=-N}^{N} a_{N\,K}^{S\,I\,\pm\,F\,\tau}\,|S\,J\,IFNK\rangle, \quad (63)$$

where the coefficients $a_{N\,K}^{S\,I\,\pm\,F\,\tau}$ are the hyperfine-spin-rotation mixing coefficients and τ is an arbitrary or energy-ordering index. This index can be conveniently (but only partially) replaced by the near-quantum numbers J and/or N, which can be recovered by localizing the maxima of the wave functions if the couplings remain weak. The coefficients $a_{N\,K}^{S\,I\,\pm\,F\,\tau}$ meet the property

$$a_{N\,-K}^{S\,I\,\pm\,F\,\tau} = \pm(-1)^{F+S+I+N+K}\,a_{N\,K}^{S\,I\,\pm\,F\,\tau}. \quad (64)$$

The block of symmetry labeled "$-$" can be identified easily because it contains the diagonal matrix element

$$\langle S, J = F, I, F, N = J - S, K = 0|\sum_{\mathcal{X}}[T_0^{(0)}(\mathcal{X}) + T_0^{(2)}(\mathcal{X})]|S, J' = F, I, F, N' = J - S, K' = 0\rangle, \quad (65)$$

where $T_0^{(0)}(\mathcal{X}) + T_0^{(2)}(\mathcal{X})$ denotes the component 0 of the zeroth- or second-order irreducible tensor of the four Hamiltonians $\mathcal{H}_{\rm rot}$, $\mathcal{H}_{\rm SR}$, $\mathcal{H}_{\rm FC}$, and $\mathcal{H}_{\rm dip}$.

The intensity of the electric dipole transition is obtained by using the usual tensor algebra [76], which allows us to determine the line strength,

$$\mathcal{S}_l^u\,\mu_{\rm band}^2 = \mathcal{S}_{S_l\,I_l\,Sy_l\,F_l\,\tau_l}^{S_u\,I_u\,Sy_u\,F_u\,\tau_u}\,\mu_{\rm band}^2 = 3\sum_{m_u=-F_u}^{F_u}\sum_{m_l=-F_l}^{F_l}|\langle\psi_{{\rm ev}_u}\,S_u\,I_u\,Sy_u\,F_u\tau_u\,m_u|\overrightarrow{\mu}\cdot\widehat{\epsilon}^*|\psi_{{\rm ev}_l}\,S_l\,I_l\,Sy_l\,F_l\,\tau_l\,m_l\rangle|^2\,\delta_{I_u I_l}\delta_{S_u S_l}$$

$$= (2F_u + 1)(2F_l + 1)\left|\sum_{J'=|F_u-I|}^{F_u+I}\sum_{J=|F_l-I|}^{F_l+I}\sqrt{(2J'+1)(2J+1)}\begin{Bmatrix}J' & F_u & I\\ F_l & J & 1\end{Bmatrix}\right.$$

$$
\times \sum_{N'=|J'-S|}^{J'+S} \sum_{N=|J-S|}^{J+S} \sqrt{(2N'+1)(2N+1)} \begin{Bmatrix} N' & J' & S \\ J & N & 1 \end{Bmatrix}
$$

$$
\times \left. \sum_{K'=-N'}^{N'} (-1)^{K'} \sum_{q} \begin{pmatrix} 1 & N & N' \\ q & K'-q & -K' \end{pmatrix} T_q^{(1)}(\mu)\, a_{l_{N\,K'-q}}^{S\,I\,Sy_l\,F_l\,\tau_l}\, a_{u_{N'\,-K'}}^{S\,I\,Sy_u\,F_u\,\tau_u} \right|^2, \tag{66}
$$

where $a_{l_{N\,K'-q}}^{S\,I\,Sy_l\,F_l\,\tau_l}$ and $a_{u_{N'\,-K'}}^{S\,I\,Sy_u\,F_u\,\tau_u}$ are the respective mixing coefficients of the lower and upper levels issued from the molecular Hamiltonian calculation. The coefficients $T_q^{(1)}(\mu)$ are the spherical tensorial components of the electric dipole moment operator μ. Due to the symmetry of the vibronic wave functions, only the component along the a axis (parallel band), $\mu_a = T_0^{(1)}(\mu)$, needs to be calculated when only totally symmetric vibrational levels belonging to the ground state are involved in the $\widetilde{A}\,^2B_2 \leftarrow \widetilde{X}\,^2A_1$ electronic transition of NO_2.

Resulting from the usual parity alternation with F, the HFWS raises optical selection rules similar to those associated with the usual Wang symmetry (pure rotor) [74,77], with the SRWS [52], or with the AIRWS [78] (see Table II). When considering the transitions showing SA, we assume that only those consisting of one single clump of the spin-rotation doublets are close enough (i.e., within the Doppler broadening) to interfere.

V. COMPUTER IMPLEMENTATION

The formalism as described in Secs. II, III, and IV has been implemented in the application "Stepram" [52,78]. It offers a graphic user interface and runs on a standard personal computer. It allows full simulation and fitting of the experimental spectra. When the line frequencies and assignments are available, transition frequency fits can be performed without the calculation of the spectrum amplitude. Fitting of the spectrum envelope (global spectrum envelope fitting, GSEF) is always more time consuming than fitting of the line frequency. It may also be barely efficient in the case of poor line amplitude matching (for example in the case of local perturbations). When the line frequency determination is required, "multiline", another custom-made application has been used. It allows fitting of set of individual transitions with normalized line profiles chosen among the following ones: Gaussian, Lorentzian, Voigt or crude saturation (i.e., assuming $\gamma_{ul} \ll \Delta_D$ [66], see Section II G 2). The fit of the absorption coefficient versus the intracavity power (see Section VII B) has been possible by running another custom-made application based on Perl/Tk. All the fit procedures call routines from

the "Minuit" package [79] whereas the integration algorithms are from the Gnu Scientific Library (GSL) [80]. The matrix diagonalization and the linear algebra algorithms are carried out by using the Perl Data Language (PDL) [81] supplemented by the PDL-LinearAlgebra package, an implementation of Lapack in Perl.

The full Hamiltonian matrices are blocked by applying modified Wang transformations which provides the relevant HFWS associated.

VI. EXPERIMENT AND DATA ACQUISITION

A. The SA-CRDS experimental setup

Only a summary of the experimental setup is reported here (see Fig. 1), as it has been described in a previous publication [11]. The injection of the cw Ti:sapphire laser beam (Coherent 899-21; spectral width < 1 MHz) into an evacuated symmetric high-finesse cavity (dual root blowers: 250 and 500 m^3/h) is accurately controlled by matching the beam with the TEM_{00} cavity transverse mode. Transverse mode matching is made possible by spatially filtering the laser beam with a diamond-coated pinhole. The central part of the diffracted beam is selected by a round aperture. Mode matching is provided by the fine adjustment of a lens mounted on a translation table and a periscope. The radius of curvature of the high-finesse cavity mirrors (from REO) and the length of the cavity together determine the shape of the TEM_{00} mode, i.e., the size of the beam waist [59]. Modulation of the laser source frequency, or of the position of one of the cavity mirrors driven by a piezoelectric transducer, allows us to visualize the different cavity modes by collecting the almost-entire cross section of the beam "leaking" out of the cavity on a silicon photodetector (Hamamatsu S3399). Elimination of the undesirable modes is obtained experimentally by adjusting the beam injection via the optomechanics devices mentioned previously. A rejection rate higher than 100:1 is easily attainable. This matching is almost-simultaneously obtained with the optimization of the finesse of the cavity (maximization of the cavity RD time). When an accurate cavity matching is obtained, a custom-made control system allows frequency-tuning a longitudinal cavity mode to the laser-beam frequency by a micromodulation of the position of one of the cavity mirrors. The frequency stabilization of the laser source remains under the control of the laser control box. Frequency scans (maximum range of ~1 cm^{-1} per scan) are performed by applying the required voltage issued from a digital-to-analog converter (DAC) to the analog external input of the laser control box.

The RD decays are acquired by using the custom-made control box, which collects the signal of the photodetector and controls the switching (on/off) of the acousto-optic

TABLE II. Optical selection rules relevant to the different types of dipole transitions between eigenlevels exhibiting a hyperfine-spin-rotation Wang symmetry.

ΔF [branch(es)]	a and b type	c type
0 (Q)	$+ \leftrightarrow -$	$+ \not\leftrightarrow -$
± 1 (P, R)	$+ \not\leftrightarrow -$	$+ \leftrightarrow -$

FIG. 1. (Color online) Schematic of the experimental arrangement for SA-CRDS. Cavity length, 0.35 m; radius of curvature of the mirrors, 0.5 m. FP, Fabry-Perot etalon; PD, photodiodes; PH, pinhole; AOM, acousto-optic modulator; BS, beam splitter ($\sim 1\%$); M, periscope mirror; A; aperture; L, lens; PZT, piezoelectric actuator.

modulator (AOM) (from AA Opto-Electronics). The AOM driver has been optimized to obtain a high rejection of the radio-frequency (RF) signal (>80 dB) when it is switched off and a fast commutation time (<200 ns) by using an RF switch and an amplifier from Mini-Circuits. The photodetector is run in the photoconductive mode; it is complemented by a fast transimpedance amplifier built on the same printed board as the photodetector. The responsivity ($\eta = 0.5$ A/W) of the photodetector and the value of the transimpedance resistor (R_F) as well as the gain of the analog-to-digital-converter (ADC) allow the determination of the EM-field intensity leaking out of the CRDS cavity. After evaluation of the transmission coefficient of the CRDS mirror ($\mathcal{T} \sim 4.5$ ppm), the power circulating inside the cavity can be monitored at any instant of the RD decay. Such an arrangement provides the complete control of the EM field intensity captured inside the cavity: a monitored and adjustable voltage threshold is used to trigger the beam shutting (through the AOM) and also to trigger the acquisition of the RD decay (through the ADC). Then the following cycle can be started by unshutting the laser beam. Let us note that the buildup time of the CRDS cavity, i.e., the time required to reach the desirable amount of power captured inside the cavity, is controlled by the characteristic time of the cavity, the mode matching, and the power delivered by the laser source. In theory, power values of several hundred kilowatts could be captured inside the cavity. However, the cavity spectral bandwidth at "resonance" is several orders of magnitude less than the laser source spectral width and the majority of the incoming EM-field intensity is just lost [the cavity free spectral range (FSR) is a lot larger than the source spectral width]. A cavity finesse of 450 000 is routinely obtained.

Because the present study focuses on quantitative nonlinear absorption processes, the linearity of the acquisition chain has been carefully checked and some weak corrections to linearity of the ADC have been numerically implemented. The RD decay data acquisition is due to a 12-bit, 5-MHz acquisition card (National Instruments). The Ti:sapphire laser is controlled by a 16-bit DAC. The entire supervision of the acquisition process is due to a custom-developed Labview virtual instrument (National Instruments).

B. Modes of operation

Two complementary modes of data acquisition have been used: (i) temporal decay acquisition at a fixed wavelength (laser frequency positioned) and (ii) spectrum acquisition. Both are discussed below.

1. Temporal decay mode

In the decay acquisition mode, thousands of decays (initialized with the same power threshold) can be averaged to improve the signal-to-noise ratio. Thus, relatively long decays (*viz.*, approximatively 10 times the characteristic cavity time) can be acquired. In the case of linear absorption (i.e., when the absorption is independent of the EM-field amplitude), the RD decay is expected to match a decaying exponential shape [11], but in the case of nonlinear absorption this handy behavior is lost. Rather, the absorption coefficient dependence versus the intracavity EM-field power is obtained from the derivative of the temporal decay. A numerical differentiation of the acquired voltage $U(t)$ is calculated. Assuming that the RD decays

can be approximated by exponential shapes controlled by a time-dependent characteristic time, we derive

$$\alpha(t) = -\left(\frac{\frac{dU(t)}{dt}}{U(t)} + \frac{1}{\tau_e}\right)\frac{l_{cav}}{cl_{sam}}, \qquad (67)$$

where τ_e is the response time of the empty cavity and l_{sam} is the absorption length of the sample (l_{cav} is the cavity length).

From the intracavity running power,

$$P(t) = \frac{U(t)}{\mathcal{T}\,\eta\,R_F}, \qquad (68)$$

a plot of $\alpha(P)$ can then be readily obtained by eliminating the variable t.

2. Spectrum acquisition mode

Because it was not actually possible either to store the individual temporal decays, with the intention of analyzing them later to cipher the absorption coefficients versus the EM-field intensity, or to run an operating mode similar to that described in Sec. VI B 1 in real time, an alternative mode has been used. Each decay or, possibly, averaged decay is analyzed in real time to accommodate typically five decay times. They are obtained by performing five linear regressions on the same number of time intervals by running a weighted logarithm of the measured voltages (the logarithm function is pretabulated and indexed to minimize the calculation time) after subtraction of the instrumental voltage offset. Each regression applies to a set of data ranging from U_0/q^i to U_0/q^{i+1}, where U_0 is the initial threshold set for the decay acquisition, and q is a numerical quantity typically equal to 2.5 (i ranging from 0 to 4); see, for example, Fig. 6 of Ref. [11]. Thus, knowing U_0 and q, and with the use of Eq. (68), a mean power value can be attributed to each data sample and associated with the RD time (τ_i) determined in real time. Finally, the absorption coefficient is deduced from

$$\alpha_i = \left(\frac{1}{\tau_i} - \frac{1}{\tau_e}\right)\frac{l_{cav}}{cl_{sam}}. \qquad (69)$$

It turns out that typically five spectra are simultaneously obtained from a single scan. This allows immediate identification of transitions exhibiting nonlinear absorption because they do not overlap each other. Extensions of the intracavity power range are easily obtained by modifying the value of the initial threshold U_0.

Simultaneously to the absorption spectra, a fluorescence signal (LIF) can be acquired by using a photomultiplier tube collecting the photons emitted by the traveling molecules [11]. Analysis of such LIF spectra has been given up because of the undecipherable amplitude of the transitions observed. However, nonlinear behaviors have been clearly identified.

VII. DATA ANALYSIS

In this paper the data analysis relies on the $^q R_0(0)$ line pattern located around 12 536.4 cm^{-1}. The full analysis and assignment of the hot band to which this pattern belongs remain undecipherable [35]. Such a line pattern is easily recognizable in a cold spectrum because of its shape (i.e., contour) and its pairing with the $^q P_0(2)$ pattern (separation

~2.53 cm^{-1} [82]). Despite the poor information available on the band assignment, validation of the formalism developed in the previous sections and determination of some relevant quantities, such as the band dipole moment, are possible.

The complete analysis is based on three main steps, described below. Actually, an iterative process was performed because inserting all the collected data into a single fitting algorithm was not an option. The majority of the parameters were determined by minimizing a least-squares sum χ^2 coefficient and by optionally weighting the data [83]. Parameters related to the EM-field power density were deduced by inferring the intracavity beam waist size.

The strong correlation of the EM-field power density with the population and coherence rates embedded in the saturation coefficient make it difficult to provide an accurate value for the band dipole moment or the number density without complementary studies. These additional studies are constrained by the lack of evidence of collisional processes inside the probed region of the slit expansion.

All the recorded spectra were frequency linearized, which was made possible by the simultaneous acquisition of the interference pattern from a solid Fabry-Perot etalon and of the NO$_2$ spectra. The frequency calibration is due to a custom-made wave meter [84] double-checked against a simultaneously acquired iodine spectrum, which is also available through PGOPHER [85] (our reference for the calibrations). Absorption coefficients were determined using formula (69) after evaluation of the characteristic time of the empty cavity (cf. $\tau_e = 152.7\ \mu$s at 12 536.4 cm^{-1}).

A. Fit of the $^q R_0(0)$ pattern

The $^q R_0(0)$ pattern is constituted of nine transitions resulting from the spin-rotation and hyperfine couplings. It has been frequency scanned in such a way that several spectra can be simultaneously obtained for different mean intracavity running power values (see Sec. VII C). Figure 2 shows a good example of the acquired data. This plot was obtained at an estimated mean power (P) of 9.3 W (first interval in the RD decay of series a; see Sec. VI B 2). The Lamb and crossover dips are clearly identifiable. Nevertheless, the shape of the $^{q0} Q_{21}(0.5)$ clump suffers from the existence of additional transitions (in the lowest frequency side) where dips are observable; they are indicated in magenta in Fig. 2. The median one is probably a crossover dip. The frequency of all the discernible dips has been obtained by fitting the pattern intensity (see Sec. V). Then, after data reduction, the frequencies of the nine transitions constituting the $^q R_0(0)$ pattern were fitted to obtain several molecular constants or combinations of constants.

A summary of the pattern analysis is reported in Table III. It lists the result of two fit processes. The first one assumes that the molecular constants of the lower state ($v_2 = 1$) are known [86], while the second set of parameters was obtained by freeing the constant a_{FC} (of the lower state). Due to the limited number of data available, only four linearly independent quantities are deductive: (i) the Fermi contact term, (ii) the spin dipolar term λ', (iii) the sum of two of the spin-rotation tensor components, and (iv) the value of the energy term $T_0' + B' + C'$ of the unidentified upper vibronic level. The value of the coefficient χ^2 drops by a factor of 3 when a_{FC} is
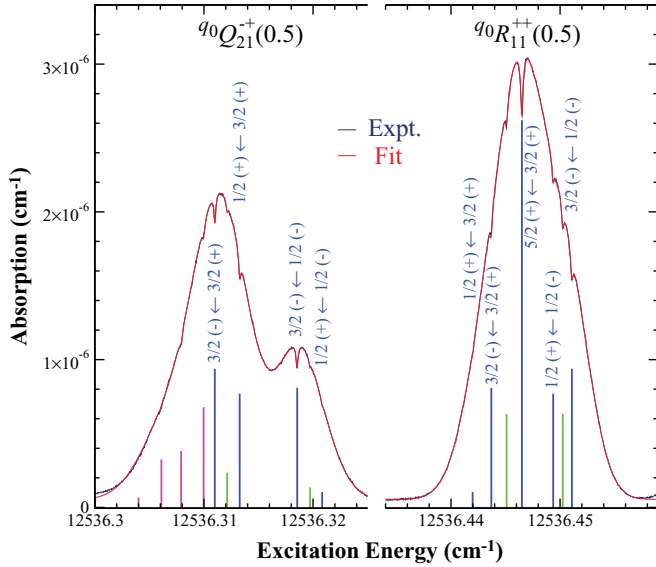
FIG. 2. (Color online) Fit of the $^q R_0(0)$ pattern matching the mean intracavity power value of 9.3 W. Experimental data are shown in dark blue, and fitted (unweighted) data in red (the two plots are almost indistinguishable). Assigned lines are indicated in blue: the values of F in the upper and lower states are given, as well as the HFWS (the relevant SRWS is also given, with the modified Mulliken notation corresponding to the spin-rotation coupling only). The lower levels have rotational symmetry A_1; the upper levels, symmetry B_1. Unassigned lines are indicated in magenta. All lines were fitted by a crude saturation profile except the crossover dips, which were fitted by a Lorentzian profile (indicated by vertical green lines). The intensity of each vertical line of the same color is to the same scale. A detailed energy level diagram is available in Ref. [41].

freed and it has motivated a report on the new determination. However, its standard deviation leads us to believe that this new value of a_{FC} is only partially relevant.

The obtained value of the spin-rotation component $(\widetilde{\epsilon}'_{bb} + \widetilde{\epsilon}'_{cc})/2$ is very close to that published by Delon and Jost [35]. The reported standard deviations of the fitted parameters have been determined by estimating a uniform uncertainty allotted to the line frequencies.

TABLE III. Molecular constants calculated from the $^{q_0}Q_{21}(0.5)$ and $^{q_0}R_{11}(0.5)$ patterns. Fitted values obtained by setting $T_0 = 749.652961$ cm^{-1}, $\lambda = 0.3716 \times 10^{-3}$ cm^{-1}, $\tau = 0.482 \times 10^{-3}$ cm^{-1} [88], and $\tau' = 0$ ($\lambda = -T_{aa}/2$, $\tau = T_{aa} + T_{bb}/2$). The χ^2_{nor} coefficient was obtained by assuming a uniform transition value uncertainty equal to 0.25×10^{-3} cm^{-1}.

	4 free parameters	5 free parameters
$T'_0 + B' + C'$	13 286.05591(10) cm^{-1}	13 286.05591(10) cm^{-1}
$\frac{\widetilde{\epsilon}'_{bb}+\widetilde{\epsilon}'_{cc}}{2} = \overline{\widetilde{\epsilon}'_{bb}}$	0.08861(13) cm^{-1}	0.08863(13) cm^{-1}
a'_{FC}	0.00326(26) cm^{-1}	0.00331(27) cm^{-1}
λ'	0.95(46) $\times 10^{-3}$ cm^{-1}	0.91(46) $\times 10^{-3}$ cm^{-1}
a_{FC}	0.00489444 cm^{-1}	0.00498(12) cm^{-1}
$\sqrt{\chi^2}$	0.219 $\times 10^{-3}$ cm^{-1}	0.116 $\times 10^{-3}$ cm^{-1}
χ^2_{nor}	0.77	0.24

B. Absorption-power dependence

Analysis of the absorption coefficient versus the intensity of the EM field can be performed by positioning the laser source frequency at the center of the strongest absorbing line in the previously analyzed pattern, that is, at the center of the strongest dip of the $^{q_0}R_{11}(0.5)$ clump located at $\widehat{\nu} \simeq$ 12 536.44649 cm^{-1} (transition, F: $5/2 \longleftarrow 3/2$). The $\alpha(P)$ plot can be obtained as explained in Sec. VI B 1. A concatenation of two RD decays covering the power range from $\sim$0.01 to $\sim$65 W is shown in Fig. 3. As mentioned previously, the line splitting resulting from the hyperfine interactions is within the Doppler broadening, giving a complex shape to the $R_{11}(0.5)$ and $Q_{21}(0.5)$ patterns (see Sec. VII A). To accurately fit the observed absorption-power dependence, all the interfering lines, including their Zeeman components, are considered [see Eq. (39)] with their associated line strengths [see Eqs. (45) and (66)]. The line Rabi frequencies are deduced from the running EM-field power and from the beam waist size, knowing the cavity length and the mirror radius of curvature [59,87]. The line frequencies are obtained using the molecular Hamiltonian provided by Eq. (56) and utilizing the molecular constants given in Table III and Ref. [88], while the line strengths are obtained from Eq. (66).

The experimental data and two fitted plots are shown in Fig. 3. Let us first note that the experimental noise is more pronounced for the lowest power values. These fluctuations result from the numerical derivative, which becomes poorly
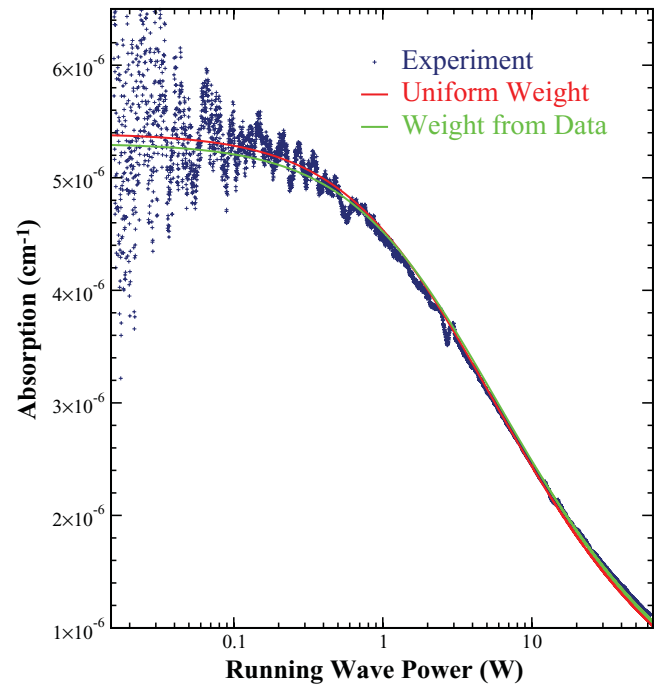

FIG. 3. (Color online) Ring-down decay converted into a power-absorption dependence plot obtained by positioning the laser source at 12 536.44649 cm^{-1}. A beam waist of 0.246 μm, a Doppler broadening (HWHM) of 0.00225 cm^{-1}, and population relaxation rates of 2.6 MHz are assumed. To calculate the derivative, the ring-down decay was averaged over a time interval of 10 μs. The two glitches observable at 2.6 and 13 W are attributed to conversion nonlinearities embedded in the ADC.

TABLE IV. Dipole moments deduced from the SA-CRDS. Values deduced from the crude model (see text) assume that absorption is only due to the transition $^{q_0}R_{11}(0.5)\,5/2 \longleftarrow 3/2$. Doppler broadening: $w_D = 0.00225$ cm^{-1} (HWHM). Relaxation rates: $\Gamma_u = \Gamma_l = \gamma_{ul} = 2.6(4)$ MHz. $\mathcal{N}_l$ is the value of the number density in the lower level [see Eq. (73)]. The lack of reported error bars results from some irrelevant standard deviations provided by the fit processes, e.g., when weighting the data with their experimental fluctuations. Only the crude mode provides a relevant value of the standard deviation and is reported here (see Table V for the final estimated error bars).

	Full model		Crude model	
	Uniform weight	Calculated weight	Uniform weight	Calculated weight
μ_{band}	0.00482 D	0.00464 D	0.00183(3) D	0.00175 D
$\mathcal{N}_l$	9.23×10^{10} cm^{-3}	9.79×10^{10} cm^{-3}	7.68×10^{11} cm^{-3}	8.23×10^{11} cm^{-3}
χ^2	6.00×10^{-14}	1.53×10^{-14}	6.07×10^{-14}	1.55×10^{-14}

determinable at the end of the time decay when the RD signal is close to 0. Taking into account the error bars derived from such amplitude fluctuations, the experimental data can be weighted with a factor inversely proportional to the square of the fluctuations, obtained by a statistical analysis of the nearest neighbor data. It turns out that such a weighting is proportional to the intracavity power.

While both weighted and "unweighted" plots of the fitted data show a good agreement with the experimental data, further inspection indicates a better match when the experimental data are nonuniformly weighted. Furthermore, we can observe that at high power, the calculated saturation is slightly too high, emphasizing the lack of simulated absorption. This slight mismatch remains unexplained and only hypotheses can be formulated since all attempts to improve the data modeling or the fitting failed. Among them, the effect of a small detuning of the laser frequency has been examined; unfortunately, it only amplifies the mentioned lack of absorption. The model used assumes that the molecules travel through a mean EM field; this means that they do not experience the spatial modulation of the stationary EM field. This modulation was included in the model without convincing results. Similar, unconvincing behavior was observed by including the transverse profile (Gaussian shape) of the EM field. Finally, we are only able to hypothesize a slight laser frequency jittering and/or the dispersion of the transit time (and, consequently, of the population relaxation rates) caused by the transverse jet expansion, i.e., by the lack of planarity of the (V shaped) jet expansion. The validity domain of the model is further questioned in Sec. VIII.

At that step in the analysis, it is relevant to compare the described formalism with a crude model. Ignoring the Zeeman sublevel complexity and assuming a single absorbing transition, the SA at the center of the line dip becomes [89–91]

$$\alpha(\omega_{ul}) = \frac{\alpha_0}{\sqrt{1 + 2\frac{P}{P_{\text{sat}}}}}, \tag{70}$$

where

$$P_{\text{sat}} = \frac{c\epsilon_0}{2} \frac{\hbar^2}{\mathcal{S}_l^u \mu_{\text{band}}^2} \frac{\gamma_{ul}}{T_1} \frac{\pi w_0^2}{2} \tag{71}$$

and

$$\alpha_0 = \frac{\pi\omega_0}{3\epsilon_0 \hbar c} \mathcal{S}_l^u \mu_{\text{band}}^2 \mathcal{N}_l \frac{1}{\Delta_D} \sqrt{\frac{\ln 2}{\pi}} \text{werf}\left(\frac{i\gamma_{ul}}{\Delta_D/\sqrt{\ln 2}}\right). \tag{72}$$

For the specific transition analyzed here, $\mathcal{S}_l^u = 2$, and

$$\mathcal{N}_l = g_{\text{ns}} \frac{e^{-\frac{E_l}{kT}} - e^{-\frac{E_u}{kT}}}{Q} \mathcal{N}_0. \tag{73}$$

The quantity werf ($\frac{i\gamma_{ul}}{\Delta_D/\sqrt{\ln 2}}$) is close to 1 since $\gamma_{ul} \ll \Delta_D$.

The final results are presented in the comparative Table IV. It shows that the values of the least square χ^2 coefficients are very similar to those obtained with the complete model when identical weightings are considered (plots which are not shown exhibit only tenuous differences from those shown). Of course, the simplicity of such a formalism, based on a single-line absorption, does not allow correct determination of the band dipole moment (a factor of $\sim$2.5 is reported) or, accordingly, of the derived number density (the products $\mu_{\text{band}}^2 \times \mathcal{N}_l$ are close, *viz.*, in the range of $\pm$10%).

C. Pattern analysis

Having determined the band strength and the relevant molecular constants, it becomes easy to simulate and eventually fit the parts of the spectrum of interest. After considering the uncertainties relative to the experimental parameters, a value of 0.0047(12) D (corresponding to an integrated absorption cross section of $\sim$9.2 $\times$ 10^{-24} cm^2/molecule) has finally been retained for the band dipole moment (see Table IV). Clumps $^{q_0}R_{11}(0.5)$ and $^{q_0}Q_{21}(0.5)$ are both considered when deriving the number density. However, the $^{q_0}Q_{21}(0.5)$ clump requires special attention because its shape is altered by unassigned transitions.

1. Linear absorption

The spectrum obtained under linear absorption conditions has to be analyzed using the same Voigt profile for each transition (data plotted in orange in Figs. 4 and 5). The $^{q_0}Q_{21}(0.5)$ clump has been fitted (GSEF) after subtracting the unassigned lines from the pattern (transition frequencies have been obtained from the analysis reported in Sec. VII A). After iterating, the value of the Lorentzian component is set to 2.6(5) MHz to match the Lamb and crossover dip width progression versus the mean intracavity power. Thus, the GSEF of both clumps allows a good determination of the residual Doppler broadening (red curve in Fig. 4).

It is worth noting that the Maxwell-Boltzmann velocity distribution along the z direction of the jet expansion (i.e., along the slit axis) does not show any noticeable deviation from
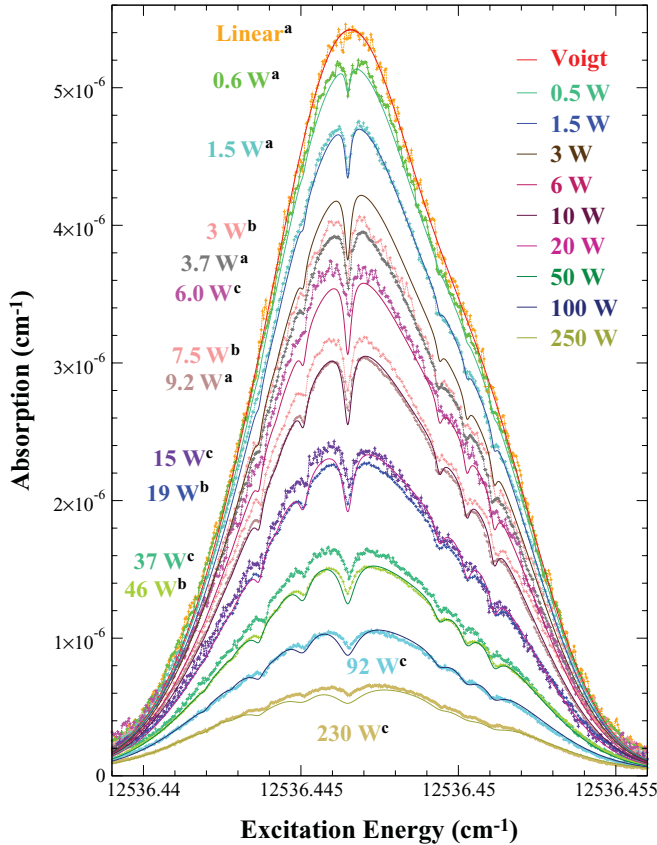
FIG. 4. (Color online) SA-CRDS of the transition (clump) $^{q0}R_{11}(0.5)$ for different values of the mean intracavity power. Spectra belonging to the same series (a, b, or c) were obtained simultaneously (average of four RD decays). Parameters relative to the line intensity used for simulations are listed in Table V, while molecular constants are reported in Table III. Experimental mean powers are indicated to the left of the patterns, while powers relative to the different simulations are indicated to the right.

FIG. 5. (Color online) SA-CRDS of the transition $^{q0}Q_{21}(0.5)$ for different values of the mean intracavity power. Color coding and captions are identical to those in Fig. 4. Unassigned lines are not simulated (left part of the figure).

the usual velocity model, whereas there is no well-established principle explaining this behavior (a supersonic circular expansion provides a totally different behavior [92,93]). A Doppler linewidth (HWHM) of 0.00225 cm^{-1} matches a thermodynamical temperature of 11.5 K for NO$_2$. This temperature is very close to the estimated rotational temperature of NO$_2$ [12(3) K] resulting from the spectral analysis of some vibronic bands of NO$_2$ not reported here.

The number density of NO$_2$ molecules has been determined and we wish to discuss its relevance. It is well known that the cooling efficiency inside a supersonic expansion is greatly dependent on the component of the kinetic energy considered [94]; *viz.*, the vibrational cooling is poorly efficient. The line intensity calculation requires us to determine the species partition function and therefore the population of all the "populated" energy levels. It follows that the partition function is easy to calculate for low temperatures but it is time-consuming for the "high" temperatures due to the large values of F. With respect to such calculations, the rotational temperatures reached inside a supersonic jet expansion are very convenient conditions. To make the calculations relative to a hot band easily tractable, we assume that the vibrational and rotational
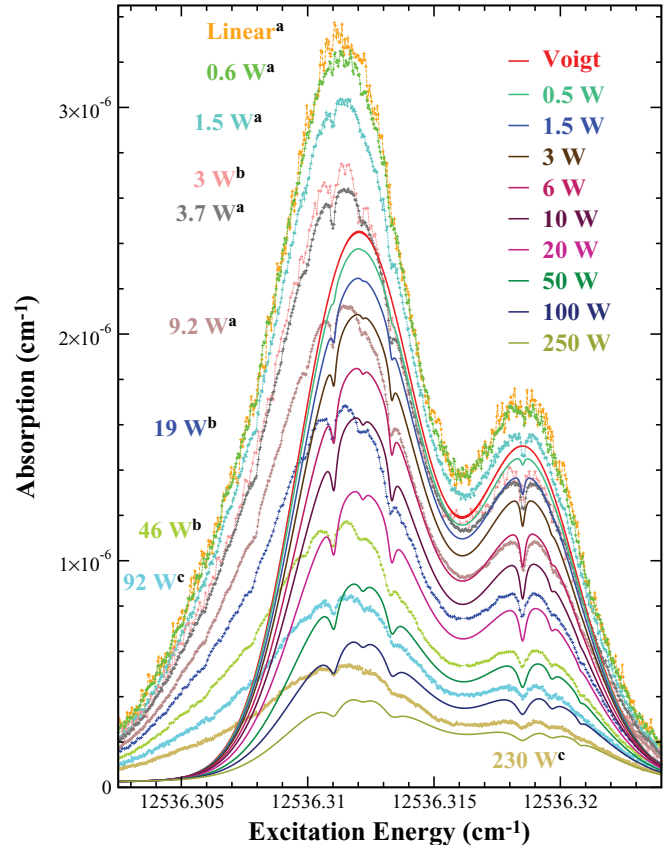
temperatures (T_{vib} and T_{rot}, respectively) are decoupled and that only a small fraction (let us say <1%) of the molecules are not in the vibrationless mode but in the $v_2 = 1$ vibrational level (Boltzmann distribution). Following this approach, only a vibrational temperature close to room temperature makes the number density of NO$_2$ molecules observed in the probed region ($\mathcal{N}_0 \simeq 3.7 \times 10^{14}$ cm^{-3}) compatible with estimations obtained from the usual model for a slit expansion [56,95]: $\mathcal{N}_0 \simeq 3.4 \times 10^{14}$ cm^{-3} (see Table V).

TABLE V. Jet expansion characterization by SA-CRDS.

μ_{band}	0.0047(12) D
	9.2(2.3) $\times 10^{-24}$ cm^{2}[a]
Δ_D (HWHM)	0.00225(7) cm^{-1}
$\Gamma_l = \Gamma_u = \gamma_{ul}$	0.087(15) $\times 10^{-3}$ cm^{-1}
$\mathcal{N}_0$ [b]	3.70(50) $\times 10^{14}$ cm^{-3}
T_{rot}	12(3) K
T_{vib}	300 K

[a]Integrated cross section: $\mathcal{N}_l \int_{\text{line}} \frac{\alpha(\omega)}{\omega_0} d\omega$.

[b]For comparative purposes, the number density estimated for a slit expansion of cross section 45 μm $\times$ 7 mm, backed at 0.5 bar (carrier gas: Ar), seeded at 1%, 3 mm downstream, is ~3.4 $\times 10^{14}$ cm^{-3}.

2. Nonlinear absorption

The analysis of the power dependence of the transition $^q R_0(0)$ is summarized in Figs. 4 and 5. We report spectra obtained when the intracavity mean power varied from ∼0 to 230 W. This was made possible by selecting three different power thresholds (see Sec. VI B 2) and gave rise to the three series, a, b, and c, indicated in the figures. It turns out that, in the medium power range, several spectra are reported with close mean power values. Visual inspection shows that some small spectral mismatches or differences can be identified. Indeed series a is the most reliable one because the highest number of data were acquired for it. For the sake of clarity, only nine spectra (excluding linear absorption) are simulated in both figures: the displayed power values are close to the experimental mean values.

Despite some small imperfect simulations, Fig. 4 shows a good match of the following features: (i) the global behavior of the absorption spectral envelope versus the intracavity power; (ii) the shape of the Lamb dips, *viz.*, their amplitude and width;[2] and (iii) the amplitude, position, and width of the crossover dips. Careful inspection shows that series b and c exhibit some small bias, probably due to the poor quality of RD decays (probably caused by noneradicated beating cavity modes). In addition, series c exhibits slight frequency shifts for a few dips, for example, around 12 536.444 cm^{-1}. This likely results from irregular frequency scans. Such irregularities are frequently observed on the scale of 10–50 MHz when using a laser source such as that operated here.

Figure 5 does not shows the same kind of agreement as Fig. 4 because of the incomplete simulation of the pattern due to the lack of line assignment as explained previously. Nevertheless, the $^{q_0} Q_{21}(0.5)$ clump consists of only four hyperfine transitions and two crossover dips (a crossover resonance can exist only if two transitions share at least one identical Zeeman sublevel), which makes the pattern relatively easy to assess.

VIII. DISCUSSION

SA spectra obtained in a high-finesse cavity have been compared with simulations based on the documented model. Despite the overall very good agreement, several mismatches can be observed by carefully inspecting the data. We wish to emphasize, first, that the reported values of the peak irradiance (up to ∼240 × 10^3 W/cm^2) cover a range of saturation running from 0 to ∼120, matching Rabi frequencies up to ∼15 MHz, and, second, that the simplified model (postulated to be relevant for low-saturation conditions) as described does not proceed with density-matrix elements involving frequencies higher than those constituting the impinging EM field, which must be considered at high saturation. Because evidence of such contributions is not clearly observed, we might claim that saturation coefficients up to 120 remain in the limit of the low-saturation regime. However, if the small deviation documented about the absorption-power dependence

at the center of a line (see Sec. VII B) is not an experimental artifact, it could be a sign that the limit of the model, as it has been reported, has been reached.

Small irregularities in the spectrum shape versus the power progression have been noted. They are observable in spectra belonging to the same scan (also the so-called series) as well as in spectra belonging to different scans. These irregularities cannot easily be accounted for because of the lack of identifiable correlations. They are ascribed to a deficiency in the control of the spectrum acquisition. Despite the automatic rejection of spurious RD decays, it is not safe to assume that the power threshold sampling issued from the RD decay analysis does not suffer from inaccuracies (cf. in the case of beating). We also wish to emphasize that the spectra were not recorded at well-established power values. But as a matter of fact, they result from absorption coefficients ciphered at power intervals covering a range of approximately ±45% of the indicated mean power.

The hypothesis of molecules crossing a mean EM field has been checked by considering the result of the spatial modulation of the EM field along the propagation and transverse directions. The clear lack of improvement afforded when implementing these additional features inclines us to believe either that the population of the traveling molecules cannot follow the spatial modulation of the EM-field beam—the molecular population relaxation rates remaining too slow to challenge such rapid changes—or that the short-time-scale micrometric motions of the cavity mirrors shake the interference pattern and raise an average value of the EM field impinging on the absorbing species. In the first case, the molecules traveling perpendicularly to the z axis ($v_z \simeq 0$) may escape from such modulation; however, their number density is too low to alter the overall behavior.

We have reported about the strong correlation between the population relaxation rates and the dipole moment sitting in the saturation coefficients. In addition, we have assumed that the probed jet expansion was exempt from collisions and that the population relaxation rates were controlled by the molecular transit time through the captured EM field. Hence the determined dipole moment may suffer from such assumptions even though these hypotheses make perfect sense. One way to obtain greater confidence in the current determinations would be to vary some of the experimental conditions. Several options are possible: (i) varying the beam waist size, for example, either by using another set of mirrors, featuring a different value of the radius of curvature, or by changing the cavity length (in the first approximation, these changes should conserve the saturation coefficients but alter the width of the dips), and (ii) changing the expanded carrier gas and thus altering the transit time and probably the residual Doppler broadening, while the rotational (and possibly vibrational) temperatures would also be modified.

As hypothesized in Sec. II C, the current model correlates the population relaxation rates and the transit time of molecules traveling through the EM field. A population relaxation rate of ∼2.6 MHz has been determined, which is twice the value derived from the transit time [see Eq. (23)] for molecules crossing the photon flow along a cross-section diameter. In other words, the effective EM-field beam waist size is $\overline{w_0} \sim$ 0.125 μm. Two explanations can be offered: (i) collisional

---

[2]The absorption at the center of the strongest Lamb dip was previously embedded in the analysis of the absorption-power dependence (see Section VII B).

processes control the relaxation rates, at least partially; and (ii) the effective population relaxation rate results from the dispersion of the transit times as mentioned in Sec. VII B. Although it is not possible to determine from the data analysis, the second hypothesis seems more plausible because of the lateral extension (V shaped) of the jet expansion. Nevertheless, collisions with the residual gas surrounding the free expansion cannot be excluded, although the molecules submitted to such relaxation should only marginally contribute to the RD signal.

The sensitivity to the transit time may question the determination of the dipole moment. A more accurate model should deal with weaker population relaxation rates and with the Gaussian spatial dependence of the EM field. An elegant way to solve this issue would be to determine the frequency response of the density-matrix elements to a nonmonochromatic field such as a Gaussian EM field. Unfortunately, in the absence of trivial analytical solutions, only a fully numerical treatment based on a sum of weighted (following a Gaussian distribution) Dirac δ functions seems feasible.

Throughout the study we have not accounted for possible spectral broadening due to the laser source spectral width (<1 MHz). Despite the intracavity EM field which is much sharper than the source spectral width, spectral fluctuations of the laser source should alter the experimental saturation profiles. However, the narrowest observed dips are of the order of 11 MHz (FWHM), obtained at a power value of 0.6 W (see Fig. 4), thus, only minor broadening effects are expected from convolution with the significantly narrower spectral width of the laser source.

The ultimate validation of the model should be carried out with a full simulation and, eventually, a fit of the transitions constituting the entire vibrational band. However, this remained impossible with the present data because of the lack of rotational assignment resulting from the strong conical intersection [34,35]

Finally, we wish to comment on the spectral resolution reached in a previous study conducted by the Stolte group (bolometric detection) [40–42] and to compare their results with those presented here. This comparison is meaningful because both studies report on the values of hyperfine constants of NO_2, both use the same laser source, and both use a supersonic jet expansion. Using bolometric detection (linear absorption), the spectral resolution is provided by the skimmed jet expansion (~12 MHz), while here the spectral resolution of the source is the ultimate limit (no skimmed jet expansion): the typical spectral width of the dips obtained at an intracavity power value of 9.3 W is ~18 MHz (FWHM). The least saturated spectra exhibit a resolution almost twice as low. Unfortunately, the accuracy of the scan linearization and calibration processes did not allow us to exploit the ultimate spectral resolution. This is probably one of the reasons why we are reporting uncertainties which are about twice as high as those reported in the previously mentioned work. The signal-to-noise ratio and/or the noise-equivalent absorption (NEA) [11] of both techniques should also have been compared. The NEA depends on the number density, band strength, and cooling efficiency. Regrettably, the rotational temperature can only be accurately determined if the analyzed spectrum contains enough assigned lines. All these quantities differ from setup to setup, which prevented further quantitative

comparisons of the two techniques. In addition, let us note that the values of the quantities a'_{FC} deduced by Stolte's group were used to evaluate the percentage of mixing of the $\widetilde{A}$ and $\widetilde{X}$ states.

IX. CONCLUSION

We have reported on a formalism to analyze the spectral shape of transitions due to a symmetric SA scheme. It leads to solve a system of coupled equations in the frequency space. The approximation of weak saturation has been considered by eliminating the interference terms of the density matrix at frequencies other than the fundamental frequencies. Assuming a standing-wave monochromatic EM field and neglecting the cross-coherences allow the system of equations to be analytically solved in the stationary (steady-state) regime. The analysis did not allow us to distinguish the dip broadenings due to the transit time of the molecule flowing through the captured photon beam from those due to possible collisional population relaxation processes, the effective population relaxation rates incorporating both effects. The full absorption profile encompasses the Bennett-Lamb and multicrossover dips which characterize the molecular absorption when (i) the species are impinged by a "strong" standing wave, (ii) the transitions share at least one level, and (iii) the frequency difference of the interfering transitions is comparable to the residual inhomogeneous broadening. The final output of the formalism displays a fractional form where we can distinguish the contribution of the absorption strength in the numerator from the dip amplitude modulations controlled by the denominator. Only a frequency detuning (or Doppler shift) integration was required. By establishing the ineffectiveness of spatial integrations demanded by the interference pattern due to the two identical counter-propagating waves, we concluded that the traveling molecules cross a mean EM field. The analysis of NO_2 experimental data required us to deal only with dual interfering transitions in a standard "V"-shape configuration (three-level system). This results from the low values of F involved in the observed energy levels and from the value of the hyperfine splittings in comparison with the residual Doppler broadening.

The model has also been faced with a qualitatively crude SA profile, i.e., an absorption coefficient proportional to a function in $(1 + 2s)^{-1/2}$. The plot and least squares coefficients could only be tenuously distinguished. However, this crude approximation failed to determine the value of the band dipole moment and the derived quantities.

The formalism is particularly well adapted to an experimental setup (such as SA-CRDS) composed of a high-finesse cavity when the captured EM radiation is entirely controlled, i.e., in space and in amplitude. The absorption coefficient and intracavity power are deduced from the nonexponential RD decay. The center of the cavity encompasses a supersonic slit expansion which has been characterized with respect to the number density and the residual Doppler broadening. A Maxwellian distribution accurately fits the shape of the molecule velocity distribution.

Spectra of the radical NO_2 have been used to validate the formalism. This required the full implementation of the spin-rotation and hyperfine couplings within a rigid asymmetric rotor Hamiltonian including the relevant Wang symmetry.

The full formalism has been implemented in the application "Stepram", which allows full simulation and fit of high-resolution spectra. By analyzing the pattern of the transition $^q R_0(0)$ of an unassigned hot band, the Fermi contact term, one term of the dipolar electronic-spin nuclear-spin interaction, the spin-rotation tensor component $\overline{\epsilon_{bb}}$ and the band origin have been deduced.

The absorption coefficient versus the intracavity running power has been accurately analyzed, (i) by positioning the laser frequency at the center of a transition (power varying from 0.01 to 65 W), and (ii) by recording tens of spectra with incident powers between $\sim$0 and 230 W. The amplitudes of the absorption profiles, of the Lamb and crossover dips, as well as their widths, are well simulated.

Numerous perturbations complicate the spectroscopy of NO_2 in the probed energy range and did not allow the assignment of the upper vibronic level. However, the vibronic band dipole moment has been determined and the number density of jet-cooled NO_2 is discussed. The SA-CRDS contrasts with the usual CRDS assuming a linear response of the absorption and providing the determination of either the absorption cross section or the number density.

The analytical solutions used for model implementation discarded possible contributions of the cross-coherence matrix elements to the absorption. While this assumption remains undocumented by full numerical simulations [96], the current satisfactory agreement between the simulated profiles and the experimental data around the crossover dips prevented us from challenging the model as approximated.

The high sensitivity of the SA-CRDS technique is only partially exploited when focusing spectroscopic studies on nonlinear absorption. Nevertheless, improvements of the noise-equivalent absorption are possible using a longer slit expansion. SA studies of transitions weaker than those reported here could be performed by increasing the intensity of the captured EM field. This would be possible by improving the control of the laser-beam injection inside the high-finesse cavity.

APPENDIX A: CROSS-COHERENCE

Equation (9) has been deduced from Eq. (6) by setting the cross-coherence terms between the two upper levels to 0. If such an approximation is omitted, slightly different equations can be obtained. Following the same approach as used to establish Eq. (17), we can get [from Eq. (7)]

$$\rho^{(\pm)}_{m_u m_{u'}}(\omega,z,\delta) = \frac{1}{2} \frac{\rho_{m_u m_l}(\omega,z,\delta) \otimes \Omega_{m_l m_{u'}}(\omega,z) - \Omega_{m_u m_l}(\omega,z) \otimes \rho_{m_l m_{u'}}(\omega,z,\delta)}{\omega_{uu'} - \omega + i\gamma_{uu'}} \tag{A1}$$

and

$$\rho^{(\pm)}_{m_l m_u}(\omega,z,\delta) = \frac{1}{2} \frac{\Omega_{m_l m_u}(\omega,z) \otimes \left[\rho_{m_l m_l}(\omega,z,\delta) - \rho_{m_u m_u}(\omega,z,\delta)\right]}{\omega_{ul} - \omega \mp \delta + i\gamma_{ul}} - \frac{1}{2} \frac{\Omega_{m_l m_{u'}}(\omega,z) \otimes \rho_{m_{u'} m_u}(\omega,z,\delta)}{\omega_{ul} - \omega \mp \delta + i\gamma_{ul}}, \tag{A2}$$

where $u \neq u'$ ($u = 1$ or 2).

To evaluate both terms we assume that the cross-coherences $\rho_{m_u m_{u'}}$ are only small contributions to the usual coherences $\rho_{m_u m_l}$. First, we can see that the matrix elements $\rho_{m_u m_{u'}}$ reach significant values only for $\omega \simeq \omega_{uu'} = |\omega_{12}|$, i.e., for frequencies close to the energy difference between the upper two levels. Thus, the coherences $\rho_{m_u m_{u'}}$ can only oscillate at frequencies close to ω_{12} with a relaxation rate Γ_u; this means that quantum beats altering the population relaxation are anticipated [97]. If we assume that the coherences $\rho_{m_u m_l}(\omega,z,\delta)$ are peaked functions around ω_{ul} (as in the absence of cross-coherence terms), the analysis of the convolution products shows that both products constituting the numerator of Eq. (A1) only take prominent values around $\delta = |\omega_{12}|/2$, i.e., when both upper levels are coherently populated. This condition is only reached in the vicinity of the crossover resonances where the coherences $\rho_{m_l m_u}$ become notably altered by the cross-coherences. Hence, a frequency modulation of the populations at ω_{12} with a maximum amplitude at the center of the crossover resonances is predicted. Because of the nature of the CRDS detection, such modulation is not observable when collecting RD decays.

APPENDIX B: FOURIER TRANSFORMATIONS

The Fourier transform is defined as follows (t refers to the time space and ω to the angular frequency space):

$$f(\omega) = \int \widehat{f}(t) e^{-i\omega t} dt, \tag{B1}$$

$$\widehat{f}(t) = \frac{1}{2\pi} \int f(\omega) e^{i\omega t} d\omega. \tag{B2}$$

The convolution product [98] in the frequency space becomes

$$f(\omega) \otimes g(\omega) = \frac{1}{2\pi} \int f(\omega') g(\omega - \omega') d\omega'. \tag{B3}$$

The Dirac δ function in the frequency space is

$$\delta(\omega) = \frac{1}{2\pi} \int e^{-i\omega t} dt. \tag{B4}$$

We deduce the convolution products involving a shift in the Dirac δ function,

$$\delta(\omega - \omega_0) \otimes g(\omega - \omega_0) = \frac{1}{2\pi} g(\omega - 2\omega_0) \qquad \text{(B5)}$$

and

$$\delta(\omega + \omega_0) \otimes g(\omega - \omega_0) = \frac{1}{2\pi} g(\omega). \qquad \text{(B6)}$$

---

[1] A. Javan, W. R. Bennett Jr., and D. R. Herriott, Phys. Rev. Lett. **6**, 106 (1961).

[2] W. R. Bennett Jr., Phys. Rev. **126**, 580 (1962).

[3] W. R. Bennett Jr., Appl. Opt. **1**, 24 (1962).

[4] W. E. Lamb Jr., Phys. Rev. **134**, A1429, (1964).

[5] S. Stenholm and W. E. Lamb Jr., Phys. Rev. **181**, 618 (1969).

[6] R. G. Brewer, M. J. Kelly, and A. Javan, Phys. Rev. Lett. **23**, 559 (1969).

[7] C. J. Bordé, in *Proceedings of the Fourth International Symposium on Frequency Standards and Metrology*, edited by A. De Marchi (Springer-Verlag, New York, 1989), pp. 196–2005.

[8] F.-L. Hong, J. Ye, L.-S. Ma, S. Picard, C. J. Bordé, and J. L. Hall, J. Opt. Soc. Am. B **18**, 379 (2001).

[9] F.-L. Hong, H. Inaba, K. Hosaka, M. Yasuda, and A. Onae, Opt. Express **17**, 1652 (2009).

[10] D. Romanini, P. Dupré, and R. Jost, Vib. Spectrosc. **19**, 93 (1999).

[11] P. Dupré, C. R. Acad. Sci. Paris, Ser. IV **2**, 929 (2001).

[12] P. Zalicki and R. N. Zare, J. Chem. Phys. **102**, 2708 (1995).

[13] L. Lehr and P. Hering, Appl. Phys. B **65**, 595 (1997).

[14] S. S. Brown, H. Stark, and A. R. Ravishankara, Appl. Phys. B **75**, 173 (2002).

[15] C. R. Bucher, K. K. Lehmann, D. F. Plusquellic, and G. T. Fraser, Appl. Opt. **39**, 3154 (2000).

[16] D. Lisak, J. T. Hodges, and R. Ciurylo, Phys. Rev. A **73**, 012507 (2006).

[17] D. Lisak, J. T. Hodges, and R. Ciurylo, Appl. Phys. B **88**, 317 (2007).

[18] G. Giusfredi, S. Bartalini, S. Borri, P. Cancio, I. Galli, D. Mazzotti, and P. De Natale, Phys. Rev. Lett. **104**, 110801 (2010).

[19] J. Y. Lee and J. W. Hahn, Appl. Phys. B **79**, 653 (2004).

[20] J. Ishikawa, F. Riehle, J. Helmcke, and C. J. Bordé, Phys. Rev. A **49**, 4794 (1994).

[21] H. R. Schlossberg and A. Javan, Phys. Rev. **150**, 267 (1966).

[22] M. S. Feld and A. Javan, Phys. Rev. **177**, 540 (1969).

[23] C. J. Anderson, J. E. Lawler, L. W. Anderson, T. K. Holley, and A. R. Filippelli, Phys. Rev. A **17**, 2099 (1978).

[24] Ch. Chardonnet and Ch. J. Bordé, Europhys. Lett. **9**, 527 (1989).

[25] S. Mandal and P. N. Ghosh, Phys. Rev. A **45**, 4990 (1992).

[26] E. J. Friedman-Hill, L. A. Rahn, and R. L. Farrow, J. Chem. Phys. **100**, 4065 (1994).

[27] L. P. Maguire, R. M. W. van Bijnen, E. Mese, and R. E. Scholten, J. Phys. B **39**, 2709 (2007).

[28] J. I. Kim, D. Haubrich, B. Klölter, and D. Meschede, Phys. Rev. A **80**, 063801 (2009).

[29] A. A. Mills, B. M. Siller, and B. J. McCall, Chem. Phys. Lett. **105**, 1 (2010).

[30] A. Delon and R. Jost, J. Chem. Phys. **95**, 5686 (1991).

[31] C. F. Jackels and E. R. Davidson, J. Chem. Phys. **64**, 2908 (1976).

[32] G. Hirsch, R. J. Buenker, and C. Petrongolo, Mol. Phys. **73**, 1085 (1991).

[33] B. Kirmse, A. Delon, and R. Jost, J. Chem. Phys. **108**, 6638 (1998).

[34] R. Georges, A. Delon, F. Bylicki, R. Jost, A. Campargue, A. Charvát, M. Chenevier, and F. Stoeckel, Chem. Phys. **190**, 207 (1995).

[35] A. Delon and R. Jost, J. Chem. Phys. **110**, 4300 (1999).

[36] G. R. Bird, J. C. Bard, A. W. Jache, J. A. Hodgeson, R. F. Curl Jr., A. C. Kunkle, J. W. Bransford, J. Rastrup-Andersen, and J. Rosenthal, J. Chem. Phys. **40**, 3378 (1964).

[37] J. M. Brown, T. C. Steimle, M. E. Coles, and R. F. Curl, Jr., J. Chem. Phys. **74**, 3668 (1981).

[38] W. C. Bowman and F. C. De Lucia, J. Chem. Phys. **77**, 92 (1982).

[39] W. Demtröder, F. Paech, and R. Schmiedl, Chem. Phys. Lett. **26**, 381 (1974).

[40] C. A. Biesheuvel, D. H. A. ter Steege, J. Bulthuis, M. H. M. Janssen, J. G. Snijders, and S. Stolte, Chem. Phys. Lett. **267**, 515 (1997).

[41] C. A. Biesheuvel, J. Bulthuis, M. H. M. Janssen, S. Stolte, and J. G. Snijders, J. Chem. Phys. **109**, 9701 (1998).

[42] C. A. Biesheuvel, J. Bulthuis, M. H. M. Janssen, S. Stolte, and J. G. Snijders, J. Chem. Phys. **112**, 3633 (2000).

[43] J. Xin and S. A. Reid, J. Chem. Phys. **112**, 10067 (2000).

[44] A. Kastler, Appl. Opt. **1**, 17 (1962).

[45] S. Haroche and F. Hartmann, Phys. Rev. A **6**, 1280 (1972).

[46] C. J. Bordé, J. L. Hall, C. V. Kunasz, and D. G. Hummer, Phys. Rev. A **14**, 236 (1976).

[47] J. Bordé and Ch.J. Bordé, J. Mol. Spectrosc. **78**, 353 (1979).

[48] P. R. Berman, P. F. Liao, and J. E. Bjorkholm, Phys. Rev. A **20**, 2389 (1979).

[49] R. S. Mulliken, Rev. Mod. Phys. **2**, 60 (1930).

[50] S. Wu, P. Dupré, P. Rupper, and T. A. Miller, J. Chem. Phys. **127**, 224305 (2007).

[51] P. R. Bunker and P. Jensen. *Molecular Symmetry and Spectrsocopy*, 2nd ed. (NRC Research Press, Ottawa, Canada, 1998).

[52] P. Dupré, J. Chem. Phys. **134**, 244308 (2011).

[53] C. C. Lin, Phys. Rev. **116**, 903 (1959).

[54] U. Fano, Rev. Mod. Phys. **29**, 74 (1957).

[55] P. Meystre and M. Sargent III, *Elements of Quantum Optics, 3rd ed*. (Springer, New York, 1998).

[56] D. G. Miller, in *Atomic and Molecular Beam Methods, Vol. 1*, edited by G. Scoles (Oxford University Press, New York, 1980), pp. 14–53.

[57] R. N. Zare, *Angular Momentum* (John Wiley & Sons, New York, 1988).

[58] J. L. Hall, C. J. Bordé, and K. Uehara, Phys. Rev. Lett. **37**, 1339 (1976).

[59] A. Yariv, *Quantum Electronics*, 2nd ed. (John Wiley & Sons, New York, 1975).

[60] K. O. Patten, J. D. Buley, and H. S. Johnston, J. Phys. Chem. **94**, 7960 (1990).

[61] O. Chesnovsky and A. Amirav, Chem. Phys. Lett. **109**, 368 (1984).

[62] C. H. Chen, S. D. Kramer, D. W. Clark, and M. G. Payne, Chem. Phys. Lett. **65**, 419 (1979).

[63] A. R. Edmonds, *Angular Momentum in Quantum Mechanics*, 3rd ed. (Princeton University Press, Princeton, NJ, 1974).

[64] M. Abramowitz and I. A. Stegun (eds.), *Handbook of Mathematical Functions* (Dover, Mineola, NY, 1972).

[65] H. Greenstein, Phys. Rev. **175**, 438 (1968).

[66] V. S. Letokhov and V. P. Chebotayev, *Nonlinear Laser Spectroscopy* (Springer-Verlag, New York, 1977).

[67] P. R. Bunker and P. Jensen, *Fundamentals of Molecular Symmetry. Chemical Physics* (IOP, Philadelphia, PA, 2005).

[68] H. W. Kroto, *Molecular Rotation Spectra* (Dover, Mineola, NY, 1992).

[69] J. M. Brown and T. J. Sears, J. Mol. Spectrosc. **75**, 111 (1979).

[70] W. Weissbluth, *Atoms and Molecules* (Academic Press, New York, 1978).

[71] R. F. Curl Jr., and J. L. Kinsey, J. Chem. Phys. **35**, 1758 (1961).

[72] S. I. Weissman, J. Chem. Phys. **22**, 1378 (1954).

[73] I. C. Bowater, J. M. Brown, and A. Carrington, Proc. R. Soc. London A **333**, 265 (1973).

[74] G. W. King, R. M. Hainer, and P. C. Cross, J. Chem. Phys. **11**, 24 (1943).

[75] W. T. Raynes, J. Chem. Phys. **41**, 3020 (1964).

[76] A. Messiah, *Quantum Mechanics* (Dover, Mineola, NY, 1999).

[77] S. C. Wang, Phys. Rev. **34**, 243 (1929).

[78] P. Dupré, J. Chem. Phys. **134**, 244309 (2011).

[79] MINUIT2 minimization package [http://seal.web.cern.ch/seal/snapshot/work-packages/mathlibs/minuit].

[80] The GNU Scientific Library [http://www.gnu.org/software/gsl/].

[81] Perl Data Language, Scientific computing with perl [http://pdl.perl.org].

[82] A. Delon, S. Heilliette, and R. Jost, Chem. Phys. **238**, 465 (1998).

[83] P. R. Bevington and D. K. Robinson, *Data Reduction and Error Analysis for the Physical Sciences*, 2nd ed. (McGraw–Hill, New York, 1992).

[84] J. Cachenaut, C. Man, P. Cerez, A. Brillet, F. Stoeckel, A. Jourdan, and F. Hartmann, Rev. Phys. Appl. **14**, 685 (1979).

[85] C. M. Western, PGOPHER, a program for simulating rotational structure [http://pgopher.chm.bris.ac.uk].

[86] A. Perrin, J.-M. Flaud, C. Camy-Peyret, B. Carli, and M. Carlotti, Mol. Phys. **63**, 791 (1988).

[87] H. Kogelnik and T. Li, Appl. Opt. **5**, 1550 (1966).

[88] A. Perrin, C. Camy-Peyret, J.-M. Flaud, and J. Kauppinen, J. Mol. Spectrosc. **130**, 168 (1988).

[89] A. Icsevgi and W. E. Lamb Jr., Phys. Rev. **185**, 517 (1969).

[90] L. Theilman and L. W. Davis, Appl. Phys. Lett. **25**, 461 (1974).

[91] W. Demtröder, *Laser Spectroscopy*, 3rd ed. (Springer-Verlag, New York, 2003).

[92] H. C. W. Beijerinck and N. F. Verster, Physica C **111**, 327 (1984).

[93] H. C. W. Beijerinck, G. H. Kaashoek, J. P. M. Beijers, and M. J. Verheijen, Physica C **121**, 425 (1983).

[94] R. Campargue, J. Phys. Chem. **88**, 4466 (1984).

[95] S. DePaul, D. Pullman, and B. Friedrich, J. Phys. Chem. **97**, 2137 (1993).

[96] V. Kruger, M. Dumont, S. Le Boiteux, Y. J. Picard, F. Chaussard and B. Attal-Trétout, Phys. Rev. A **64**, 012716 (2001).

[97] S. Haroche, in *High-Resolution Laser Spectroscopy, Vol. 13. Topics in Applied Physics*, edited by K. Shimoda (Springer-Verlag, New York, 1976), pp. 253–313.

[98] F. W. Byron Jr., and R. W. Fuller, *Mathematics of Classical and Quantum Physics* (Dover, Mineola, NY, 1992).